

1     **High-resolution simulations of the plume dynamics in**  
2     **an idealized 79°N Glacier cavity using adaptive vertical**  
3     **coordinates**

4     **Markus Reinert<sup>1</sup>, Marvin Lorenz<sup>1</sup>, Knut Klingbeil<sup>1</sup>, Bjarne Büchmann<sup>2</sup>,**  
5     **Hans Burchard<sup>1</sup>**

6     <sup>1</sup>Leibniz Institute for Baltic Sea Research Warnemünde, Seestr. 15, 18119 Rostock, Germany

7     <sup>2</sup>Joint GEOMETOC Support Center, Danish Defence Acquisition and Logistics Organization (DALO),  
8     Lautrupbjerg 1-5, 2750 Ballerup, Denmark

9     **Key Points:**

- 10     • Melting of the 79° North Glacier ice tongue by turbulent ocean currents is stud-  
11     ied with an idealized 2D-vertical fjord model
- 12     • The subglacial plume behaves like an entraining plume close to the grounding line  
13     and like a detraining gravity current further downstream
- 14     • A vertical resolution finer than 1 m is achieved in the subglacial plume by using  
15     adaptive vertical coordinates that zoom to stratification

---

Corresponding author: Markus Reinert, [markus.reinert@io-warnemuende.de](mailto:markus.reinert@io-warnemuende.de)

**Abstract**

For better projections of sea level rise, two things are needed: an improved understanding of the contributing processes and their accurate representation in climate models. A major process is basal melting of ice shelves and glacier tongues by the ocean, which reduces ice sheet stability and increases ice discharge into the ocean. We study marine melting of Greenland’s largest floating ice tongue, the 79° North Glacier, using a high-resolution, 2D-vertical ocean model. While our fjord model is idealized, the results agree with observations of melt rate and overturning strength. Our setup is the first application of adaptive vertical coordinates to an ice cavity. Their stratification-zooming allows a vertical resolution finer than 1 m in the entrainment layer of the meltwater plume, which is important for the plume development. We find that the plume development is dominated by entrainment only initially. In the stratified upper part of the cavity, the subglacial plume shows continuous detrainment. It reaches neutral buoyancy near 100 m depth, detaches from the ice, and transports meltwater out of the fjord. Melting almost stops there. In a sensitivity study, we show that the detachment depth depends primarily on stratification. Our results contribute to the understanding of ice–ocean interactions in glacier cavities. Furthermore, we suggest that our modeling approach with stratification-zooming coordinates will improve the representation of these interactions in global ocean models. Finally, our idealized model topography and forcing are close to a real fjord and completely defined analytically, making the setup an interesting reference case for future model developments.

**Plain Language Summary**

The global increase of sea levels is a consequence of human-induced climate change. It presents a threat to coastal regions and demands action to protect human life and infrastructure near the coast. Planning protective measures requires projections of sea level rise, computed with climate models. We present an approach to improve the simulation of an important contributor to sea level rise: melting of floating ice shelves by ocean circulation. Our modeling approach uses a vertical model grid that evolves over time. The temporal evolution depends on the density structure of the ocean. Large density differences appear just below an ice shelf, where fresh meltwater mixes with salty seawater. The adaptive grid of our model resolves this mixing process in great detail. This is important for an accurate computation of the melt rate and enables us to study in depth the ice shelf–ocean interactions. We study them at the glacier tongue of the 79° North Glacier, which is Greenland’s largest ice shelf. The physical understanding gained from our simulations is also applicable to other floating glacier tongues and ice shelves. We suggest that using the presented model technique in global ocean models can improve projections of melting and sea level rise.

**1 Introduction**

Sea level rise is a consequence of human-induced climate change and a threat to coastal communities all around the world (IPCC, 2022). To protect human life and infrastructure in coastal areas, measures must be taken, ideally planned well in advance (IPCC, 2022). This requires reliable projections of sea level rise, which depend on the accuracy of climate models as well as on the understanding of the processes contributing to sea level rise. With a contribution of about 20 %, melting of the Greenland Ice Sheet is one of the main processes (Horwath et al., 2022) and the focus of this paper.

The Greenland Ice Sheet, which has the potential to increase sea levels globally by more than 7 m (Aschwanden et al., 2019), discharges into the ocean at so-called outlet glaciers. Some of these glaciers form ice tongues that float on the water and cover their fjords (Straneo & Cenedese, 2015). Greenland’s largest floating glacier tongue is currently the one of the 79° North Glacier (79NG; Schaffer et al., 2020). It is one of the three main

66 outlets of the Northeast Greenland Ice Stream (Schaffer et al., 2017; Kappelsberger et  
 67 al., 2021), holding 1.1 m sea-level equivalent of ice (*i.e.*, its ice could lift global sea lev-  
 68 els by 1.1 m if melted entirely, Christmann et al., 2021). Schaffer et al. (2020) estimated  
 69 that 89% of the meltwater leaving the 79NG fjord comes from subglacial melting caused  
 70 by the ocean. Ice melting on land or at the surface only accounts for the remaining 11%  
 71 of 79NG meltwater (and even less at other glaciers, see Rignot & Steffen, 2008), which  
 72 is discharged into the fjord as subglacial runoff at the grounding line. Subglacial melt-  
 73 ing thins the glacier tongue, which can reduce the buttressing of the ice sheet, *i.e.*, the  
 74 support of the grounded glacier that is provided by the friction between the ice tongue  
 75 and the lateral fjord boundaries (Goldberg et al., 2009). With a thinner ice tongue, thus  
 76 less buttressing, the glacier can flow faster into the ocean, which contributes to sea level  
 77 rise (Shepherd et al., 2004; Goldberg et al., 2009; Humbert et al., 2022). Furthermore,  
 78 basal melting can destabilize the ice tongue, which can lead to its breakup (Rignot &  
 79 Steffen, 2008); in consequence, a lot of ice would be discharged into the ocean (Shepherd  
 80 et al., 2004). This exemplifies the big role of the ocean in melting the Greenland Ice Sheet  
 81 (Schaffer et al., 2017) and shows that it is important to understand ice sheet–ocean in-  
 82 teractions in glacier fjords like the one at 79° North.

83 The general idea of ice–ocean interactions under a glacier tongue in Greenland is  
 84 as follows: Atlantic Intermediate Water (AIW) flows over a sill at the fjord entrance into  
 85 the glacier cavity as a dense, saline, and warm bottom plume. AIW brings heat into the  
 86 ice cavity, which is used for melting. The meltwater forms a buoyant plume on the un-  
 87 derside of the glacier tongue. This plume causes subglacial melting, transports glacially  
 88 modified water towards the open ocean, and constitutes the return flow of an overturning  
 89 circulation within the fjord (Straneo & Cenedese, 2015; Schaffer et al., 2020).

90 The dense bottom plume and the buoyant subglacial plume are the two main pro-  
 91 cesses in a glacier cavity. However, they are difficult to study, because measurements in  
 92 Greenland’s fjords are generally sparse (Straneo & Cenedese, 2015), particularly under  
 93 floating ice tongues, where the ocean is inaccessible to ships and unobservable by satel-  
 94 lites. Ice tethered moorings (Lindeman et al., 2020) give some information about pro-  
 95 cesses under the ice, but only at single positions. So numerical models in combination  
 96 with measurements are necessary to gain a detailed understanding of ice sheet–ocean in-  
 97 teractions. This requires that the model formulations properly incorporate the classi-  
 98 cal relations for stratified boundary layer flow. Baines (2008) distinguished between two  
 99 such features: gravity currents and plumes. Gravity currents have relatively gentle slopes;  
 100 they are characterized by sharp interfaces and a balance between buoyancy force and bed  
 101 friction. These gravity currents show detrainment and intrude into the ambient water.  
 102 In contrast to that, plumes exist on steeper topography; the buoyancy force is balanced  
 103 by strong entrainment of ambient water. We will show that both states, gravity currents  
 104 and plumes, exist under the 79NG ice tongue at different locations. For the turbulence  
 105 closure model used here, Arneborg et al. (2007) showed that it well resolves entrainment  
 106 rates of dense bottom currents in the Baltic Sea. This is due to the fact that the tur-  
 107 bulence closure model has been properly calibrated to reproduce a steady-state Richard-  
 108 son number of 0.25 (Burchard & Baumert, 1995; Umlauf & Burchard, 2005) and a mix-  
 109 ing efficiency of 0.2 (Umlauf, 2009; Burchard & Hetland, 2010).

110 A challenge for ocean models is to provide sufficiently high resolution in a glacier  
 111 fjord to accurately simulate the two plumes. The melt rate computed by the model also  
 112 depends strongly on the vertical resolution (Gwyther et al., 2020). It has been shown  
 113 that the subglacial plume and particularly its entrainment layer require a vertical res-  
 114 olution of about 1 m or better to correctly model the plume development and the asso-  
 115 ciated melting (Burchard et al., 2022). This is hard to achieve in most ocean models,  
 116 because of the stark contrast in vertical scales between the fjord depth of several hun-  
 117 dred meters and the plume thickness on the order of one to ten meters.

118 With the vertical coordinates that are commonly used in ocean models, it is un-  
119 feasible to achieve a resolution of 1 m along the whole subglacial plume. At 79NG, the  
120 plume starts at the grounding line at 600 m depth, so  $z$ -coordinate models (Losch, 2008)  
121 would require at least 600 vertical layers to resolve the top 600 m of the water column  
122 with a 1 m-resolution – much more than can typically be afforded in global models. Such  
123 a resolution is currently only feasible at the fjord scale, as shown in the semi-realistic model  
124 by Xu et al. (2013) for a Greenlandic glacier without an ice tongue. With  $\sigma$ -coordinates  
125 (Timmermann et al., 2012; Gwyther et al., 2020), a high resolution along the whole ice  
126 tongue is possible with less layers by activating a zooming towards the ice–ocean inter-  
127 face. However, these terrain-following coordinates have problems when calculating the  
128 internal pressure gradient over steep topographic slopes (Haney, 1991; Burchard & Pe-  
129 tersen, 1997), which are a typical feature in glacier fjords.

130 With adaptive vertical coordinates (AVC; Hofmeister et al., 2010), the described  
131 problems can be considerably reduced. AVC are terrain-following coordinates that al-  
132 low with a moderate number of layers a high vertical resolution in places of interest. By  
133 minimizing a cost function, AVC adapt automatically to features like stratification, shear,  
134 and interfaces (Burchard & Beckers, 2004). This reduces numerical mixing (Klingbeil  
135 et al., 2014; Gräwe et al., 2015) and puts more layers in places where more details need  
136 to be resolved, while permitting less vertical resolution in more uniform areas. These co-  
137 ordinates have been used successfully for simulating dense and buoyant plumes in var-  
138 ious conditions (e.g., Umlauf et al., 2010; Chegini et al., 2020), but not yet for glacier  
139 fjord modeling.

140 In this paper, we will show that the stratification-zooming feature of AVC is use-  
141 ful for modeling the ocean circulation under ice shelves, because this provides a high ver-  
142 tical resolution of 1 m in the subglacial plume and the bottom plume with feasible com-  
143 putational cost. Furthermore, we will present the new insights into the plume dynam-  
144 ics that were gained by using a model that provides such resolution.

145 We created an idealized 2D-vertical simulation of the 79NG fjord using AVC to-  
146 gether with a melt parametrization (Burchard et al., 2022) that is suitable for high ver-  
147 tical resolution at the ice–ocean interface. To our knowledge, this is the first model to  
148 use stratification-zooming coordinates like AVC in a glacier cavity. In addition to test-  
149 ing the performance of AVC under an ice tongue, we use our model to study the sensi-  
150 tivity of the 79NG system to environmental influences. With the 20 scenarios of our sen-  
151 sitivity study, we analyze the effect of the salinity and temperature stratification of the  
152 ambient ocean, test the importance of the subglacial discharge, examine the role of the  
153 sill, and investigate the influence of roughness or smoothness of the ice tongue.

154 This paper is organized as follows. The following Section 2 describes our model setup,  
155 compares it to the real 79NG fjord, explains our modeling choices including AVC, and  
156 describes our analysis methods. Section 3 shows the results of our default simulation (Sec-  
157 tion 3.1), the performance of AVC (Section 3.2), and the results of our sensitivity study  
158 (Section 3.3). This is followed in Section 4 by a discussion of the physical processes we  
159 observe in all our numerical experiments and what we learn from these findings about  
160 ice–ocean interactions in glacier cavities. We also discuss the role of AVC in obtaining  
161 the presented results. Some conclusions and an outlook are given in Section 5. Appendix  
162 A lists the mathematical expressions used to build our idealized setup, so that our model  
163 can serve as a reference test case for future model developments.

## 164 2 Methods

### 165 2.1 Idealized 2D model of the 79°N Glacier fjord

166 We built an idealized numerical ocean model of the 79° North Glacier (79NG) fjord  
 167 located in Northeast Greenland, using GETM, the General Estuarine Transport Model  
 168 (Burchard & Bolding, 2002). This model is suitable for our purpose, because

- 169 1. GETM comes with adaptive vertical coordinates (AVC) that allow high vertical  
 170 resolution in areas of interest for low computational cost (Section 2.3);
- 171 2. GETM includes state-of-the-art vertical turbulence closure with GOTM (Burchard  
 172 et al., 1999; Umlauf & Burchard, 2005; Li et al., 2021);
- 173 3. GETM has been developed specifically for the coastal ocean and estuaries (Klingbeil  
 174 et al., 2018).

175 A glacier fjord is a special type of estuary, in which the subglacial discharge plays the  
 176 role of a river in a classical estuary (Straneo & Cenedese, 2015; Muilwijk et al., 2022).  
 177 However, the main source of freshwater is not the subglacial discharge, but the subglacial  
 178 melting of the floating ice tongue (Schaffer et al., 2020). Since this is the first time that  
 179 GETM is used for simulating a glacier fjord, we extended the model to include ice tongues  
 180 and basal melting. The details of this new GETM feature are explained in Section 2.2.

181 The GETM setup presented here is a two-dimensional ( $x, z$ ) representation of the  
 182 79NG fjord with high resolution along the fjord ( $x$ ) and in the vertical ( $z$ ), but integrated  
 183 in cross-fjord direction ( $y$ ). The fjord circulation is expected to vary also across the fjord  
 184 (Lindeman et al., 2020), so a 2D model is a simplification and we discuss its implications  
 185 in Section 4. However, our 2D approach is a useful starting point, as it has the neces-  
 186 sary complexity to learn a lot about the plume dynamics and the overturning circula-  
 187 tion in the ice cavity.

188 We consider the main glacier terminus of 79NG, without the adjacent Dijnphna  
 189 Sund (Fig. 1a). The ice tongue is about 75 km long and 20 km wide; our model has the  
 190 same width ( $L_y = 20$  km) and twice the length ( $L_x = 150$  km), to have a sufficiently  
 191 large “buffer” between the glacier cavity – which is our main interest – and the open ocean  
 192 boundary. We resolve the domain with 300 water columns in  $x$ -direction ( $\Delta x = 500$  m)  
 193 and one grid point in  $y$ -direction; the resolution in  $z$ -direction with 100 adaptive layers  
 194 is explained in Section 2.3. At this horizontal resolution, neither nonhydrostatic effects  
 195 associated with the plumes nor nonhydrostatic internal waves are resolved, so it is ap-  
 196 propriate to use GETM in hydrostatic mode (Klingbeil & Burchard, 2013).

197 To construct the bottom topography of our idealized 79NG model, we look at two  
 198 datasets (Fig. 1). The seismic depth soundings by Mayer et al. (2000) are the most ac-  
 199 curate measurements of the bathymetry in the part of the fjord that is covered by the  
 200 ice tongue. The retreat of the ice tongue in recent decades facilitated more detailed bathymetry  
 201 measurements near the fjord entrance. In their bathymetric survey, Schaffer et al. (2020)  
 202 showed that the fjord is separated from the open ocean by a sill that is 325 m deep on  
 203 its deepest point. Since this sill depth is not representative for the whole width of the  
 204 fjord (Fig. 1a), we use a shallower sill in our idealized 2D model (Fig. 1b). It is at 300 m  
 205 depth in our default setup; in our sensitivity study, we analyze the effect of the sill by  
 206 varying its depth from 200 m to 450 m (Section 3.3.4).

207 The bathymetry of our idealized model is a smooth concatenation of simple, an-  
 208 alytical functions (Fig. 1b): A third-order polynomial connects the grounding line (600 m  
 209 depth) with the deepest point in the trough (900 m) and continues until it reaches a slope  
 210 of 2.5%. It is then connected linearly to the parabola forming the sill with its maximum  
 211 (300 m) at 80 km from the grounding line. The parabolic sill goes over into an exponen-  
 212 tially decreasing shelf that converges towards a depth of 450 m far offshore. The math-

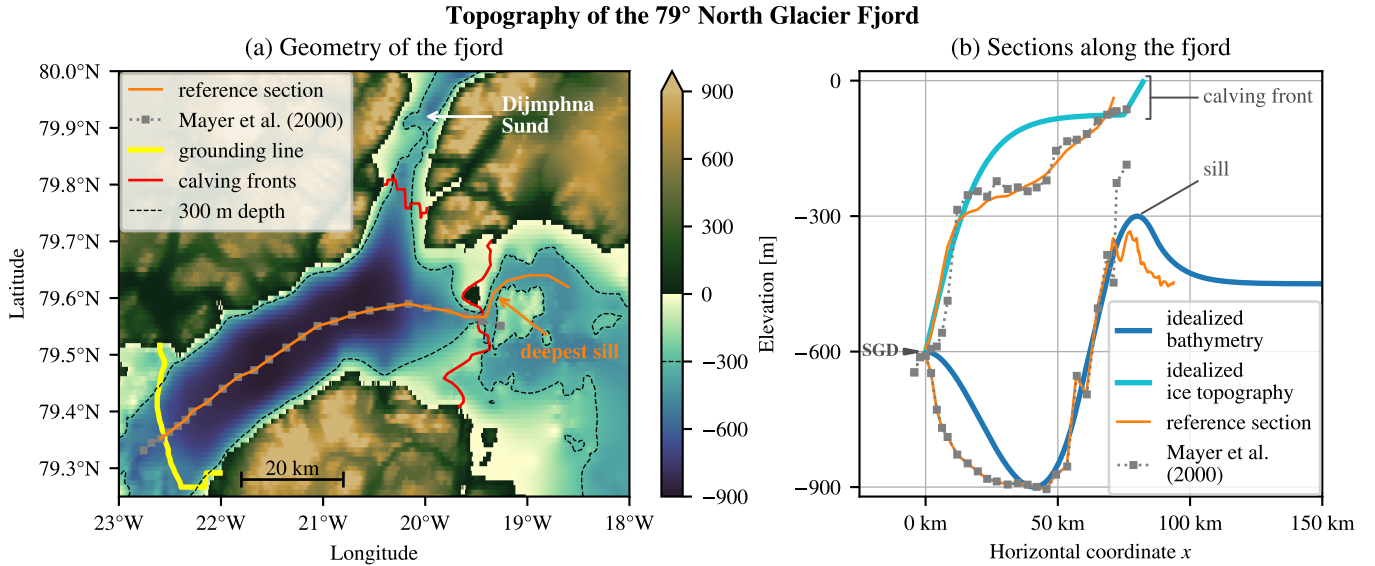


**Figure 1.** (a) Map of the 79NG fjord and its surroundings showing the bottom elevation from the RTopo-2.0.4 dataset (Schaffer et al., 2019, resolution  $30'' = 1/120^\circ$ ) together with the positions of seismic depth soundings by Mayer et al. (2000) (measured in 1997/1998 and published by Mayer et al., 2018). The floating ice-tongue extends from the grounding line in the Southwest to the northern calving front in the Dijnphna Sund and to the main calving front in the East. Atlantic water must pass over a 325-m-deep sill (labeled deepest sill) to flow from the open ocean into the cavity. The reference section is a path from the grounding line towards the open ocean that follows the depth soundings up to the calving front and passes over the deepest sill. (b) Bathymetries and ice topographies along the reference section (from RTopo), along the section by Mayer et al. (2000), and in our idealized 2D fjord model. The position where subglacial discharge (SGD) enters the cavity is marked with a wedge. Note that the deepest sill is the shallowest point along the reference section. The sill depth in our default setup (b) is 300 m, shown as a thin dashed contour in (a).

213 ematical details are given in Appendix A1. In our sensitivity experiment without a sill,  
 214 the linear slope is directly connected with the exponential shelf. Apart from the sill, our  
 215 model bathymetry only differs markedly from the measured section between the ground-  
 216 ing line and the trough (Fig. 1b). Despite this difference, we think that a simpler bathymetry  
 217 with fewer parameters is preferable to a perfect fit to a single transect for an idealized  
 218 model such as ours. Also, this deep part of the fjord is mostly inactive in our simulations.

219 At the grounding line, which forms the left/western boundary of our model ( $x =$   
 220  $0$ ), subglacial discharge enters the glacier fjord. This runoff is implemented in our GETM  
 221 setup like river input. It is added as freshwater at the local freezing point ( $-0.45^\circ\text{C}$ , which  
 222 is less than  $0^\circ\text{C}$  due to pressure) to the first water column. We take a constant discharge  
 223 rate of  $70\text{ m}^3\text{ s}^{-1}$  (equivalent to  $0.07\text{ mSv}$  reported by Schaffer et al., 2020) in our default  
 224 setup and varied this value in our sensitivity study (Section 3.3.3). The discharge is dis-  
 225 tributed uniformly over the whole water column, which is about 6.3 m thick at the first  
 226 grid center.

227 At the open boundary on the right/eastern end of our model domain ( $x = L_x =$   
 228  $150\text{ km}$ ), we prescribe the surface elevation  $\eta$  and the ambient ocean stratification. For  
 229 the former, we use a constant zero elevation. We also tested forcing the model with an

230 M2 tidal oscillation of 0.5-m-amplitude, as measured by Christmann et al. (2021), but  
 231 our experiments showed that the melt rate is relatively unaffected by the tidal forcing.  
 232 This is because in the deep part of the fjord, where the subglacial plume causes melt-  
 233 ing, the speed of the tidal currents is less than  $0.01 \text{ m s}^{-1}$  in absolute value, thus much  
 234 smaller than the plume velocity of about  $0.2 \text{ m s}^{-1}$ . Therefore, the tide is neglected in  
 235 the present study. Regarding the open boundary stratification, we use idealized and constant-  
 236 in-time profiles of temperature and salinity. They are specified by  $T$ - and  $S$ -values at  
 237 sea level, at 100 m depth, and at 300 m depth (shown in Fig. 2 and listed in Appendix A3),  
 238 using linear interpolation in between and constant extrapolation below. In our default  
 239 setup, the resulting profiles are close to CTD measurements by Schaffer et al. (2020), see  
 240 the comparison in Fig. 2. We also perform a sensitivity study with modified stratifica-  
 241 tions (Sections 3.3.1 and 3.3.2).

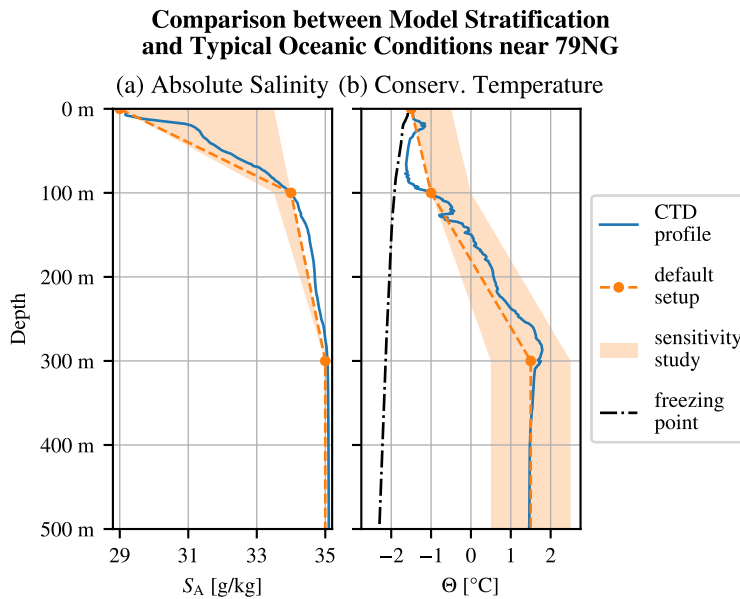


**Figure 2.** Stratification used in our model as boundary and initial conditions compared with salinity (a) and temperature (b) measurements near the 79NG fjord. The shaded area marks the minimum and maximum values tested in our sensitivity study. The CTD profile was taken in 2017 on RV *Polarstern* (Kanzow et al., 2018) and represents a typical ambient ocean stratification for 79NG (Schaffer et al., 2020, see their Fig. 1a for the location of the profile). The freezing point of saline water in (b) corresponds to the shown CTD profile. We used the Python package gsw (TEOS-10; IOC et al., 2010) to convert from the CTD data pressure to depth, practical salinity to Absolute Salinity, and potential temperature to Conservative Temperature, as well as to compute the freezing temperature.

242 The model is initialized at rest with a homogeneous stratification equal to the strat-  
 243 ification at the open boundary. We run the model with a timestep for the barotropic mode  
 244 of  $\Delta t = 5 \text{ s}$ , in accordance with the CFL stability criterion, demanding  $\Delta t \leq \Delta x / \sqrt{gH_{\max}} \approx$   
 245  $5.3 \text{ s}$  (using  $H_{\max} = 900 \text{ m}$  as the maximum depth of the fjord, see Fig. 1, ignoring the  
 246 ice cover). We use a split factor of  $M = 3$ , so that the baroclinic mode is computed ev-  
 247 ery  $\Delta t_{3D} = M\Delta t = 15 \text{ s}$ . While our default setup can be run with a larger baroclinic  
 248 timestep, the high-melt scenarios give smoother results with a higher temporal resolu-  
 249 tion, so we decided to use this split factor for all our runs. For the turbulence closure,  
 250 our setup uses the  $k$ - $\epsilon$  model with quasi-equilibrium second-moment closure (Cheng et

**Table 1.** Settings and parameters of our model in the default scenario

Name of the parameter	Symbol	Value
<b>Geometry:</b>		
length of the fjord	$L_x$	150 km
width of the fjord	$L_y$	20 km
roughness length of the sea floor	$z_0$	$1.5 \times 10^{-3}$ m
roughness length of the ice tongue	$z_{0,\text{ice}}$	$1 \times 10^{-2}$ m
<b>Glacier:</b>		
ice temperature	$T_i$	$-20$ °C
ice density	$\rho_i$	$920 \text{ kg m}^{-3}$
subglacial discharge	$Q$	$70 \text{ m}^3 \text{ s}^{-1}$
<b>Numerics:</b>		
vertical model layers		100
horizontal resolution	$\Delta x$	500 m
barotropic timestep	$\Delta t$	5 s
baroclinic timestep	$\Delta t_{3D}$	15 s
divergence damping	$A_n$	$50 \text{ m}^2 \text{ s}^{-1}$
<b>Thermodynamics:</b>		
heat capacity of sea water	$c$	$3985 \text{ J kg}^{-1} \text{ K}^{-1}$
heat capacity of glacial ice	$c_i$	$1995 \text{ J kg}^{-1} \text{ K}^{-1}$
latent heat of fusion	$L_i$	$3.33 \times 10^5 \text{ J kg}^{-1}$

251 al., 2002), implemented in GOTM. We activated divergence damping with a diffusion  
 252 of  $A_n = 50 \text{ m}^2 \text{ s}^{-1}$  on barotropic transports for a conservative smoothing of the sea sur-  
 253 face (Vallis, 1992). After a few simulation months, our model approaches a quasi-steady  
 254 state, in which melting and circulation are almost time-independent. The results shown  
 255 in this paper are 24 h-averages taken at the end of a six-month simulation and represent  
 256 the steady state.

## 257 2.2 Implementation of glacier ice in GETM

258 For this study, we added a new feature to GETM that allows simulations of glacier  
 259 fjords covered by an ice tongue. Where the ice tongue is present, it adds additional pres-  
 260 sure (Section 2.2.1), friction (Section 2.2.2), and melt fluxes (Section 2.2.3) to the sea  
 261 surface. Our implementation allows the ice to move freely vertically, for example with  
 262 long waves, but it is fixed horizontally. Calving is not included in our model.

263 In this paper, we use the term *sea surface* to refer to the (moving) upper bound-  
 264 ary of the ocean, denoted  $\eta = \eta(x, t)$  and measured from  $z = 0$  with positive values  
 265 upwards. Depending on the  $x$ -position, the sea surface can be the ice–ocean interface or  
 266 the atmosphere–ocean interface. Furthermore, we use the term *sea level* to refer to the  
 267 level  $z = 0$ , which is the initial position of the atmosphere–ocean interface.

### 268 2.2.1 Pressure due to ice and initial sea surface elevation

269 Under glacier ice, the pressure at the ice–ocean interface is the atmospheric pres-  
 270 sure (constant in our model) plus the contribution from the weight of the ice tongue (Losch,  
 271 2008). We can represent this pressure due to floating ice as  $p_i = g\rho_i h_i$ , where  $h_i$  is the  
 272 thickness of the ice column and  $\rho_i$  its (homogeneous) density (Table 1). Both  $h_i(x)$  and  
 273  $\rho_i$  are constant-in-time in our implementation and serve as input parameters to the model.

274 To initialize our model in an equilibrium state, we must prescribe the initial sur-  
 275 face elevation  $\eta_0 = \eta(t = 0)$  such that the ocean with the floating glacier ice is in hy-  
 276 drostatic balance. This is the case if the water displaced by the ice tongue has the same  
 277 weight as the ice tongue (Archimedes' principle). For an initially horizontally homoge-  
 278 neous stratification with (water) density  $\rho(z)$ , this condition can be expressed as:

$$279 \quad \rho_i h_i = \int_{\eta_0}^0 \rho(z) dz. \quad (1)$$

280 In our setup, we prescribe the lower ice edge  $\eta_0$  (see below) and determine  $h_i$  such that  
 281 (1) is fulfilled, which has the consequence that we have slightly different ice thicknesses  
 282  $h_i$  for different stratifications  $\rho(z)$  (difference to the default setup is always less than 20 cm).  
 283 Note that a corollary of (1) is the handy rule-of-thumb  $\eta_0 \approx -0.9h_i$ , which says that  
 284 90 % of an ice column is below sea level and 10 % is above.

285 Given the initially horizontally homogeneous (and stable) ocean stratification, we  
 286 initialize the ice in the chosen equilibrium position by evaluation of the integral in (1),  
 287 which yields the ice thickness and thus the pressure loading. This pressure loading is main-  
 288 tained throughout the simulation. However, as the simulation runs, the stratification changes  
 289 due to basal melting, subglacial discharge, ambient water inflow, and mixing, so the equi-  
 290 librium position of the ice changes as well. Since the ice in our model can move freely  
 291 vertically with the convergence and divergence of transports, it will adapt to the chang-  
 292 ing stratification. The setups presented here reach a quasi-steady state, in which the glacier  
 293 tongue has found a new equilibrium position, which is slightly (on the order of millime-  
 294 ters) different from the initial position.

295 In our idealized 79NG fjord model, we prescribe a smooth ice–ocean interface be-  
 296 tween the grounding line at 600 m depth and the calving front at  $x = 75$  km, where the  
 297 ice–ocean interface is 75 m below sea level. For the idealized ice shape, we choose a hy-  
 298 perbolic tangent with a maximum slope of 2.5 % at the grounding line (see Appendix A2  
 299 for the mathematical details). This fits well with the measured ice slope near the ground-  
 300 ing line (see the reference section in Fig. 1b). Since subglacial melting is strongest in this  
 301 area (Schaffer et al., 2020), we believe it is important to reproduce the ice topography  
 302 well near the grounding line and accept that the idealized shape differs from observa-  
 303 tions at mid-depths, as we prefer a simple, analytical ice shape over a perfect fit to a sin-  
 304 gle transect.

305 At the calving front, a big slope is to be avoided, as it would cause problems with  
 306 the terrain-following coordinates, because the water near the calving front is strongly strat-  
 307 ified, so individual grid cells would span a large density range. Therefore, we extend the  
 308 ice–ocean interface with a linear 1 %-slope until sea level is reached. We also tested higher  
 309 slopes at the calving front, but the model results were poorer, because the horizontal flow  
 310 below the calving front was too much diluted by passing through too many cells. Thus,  
 311 we use a slope instead of a vertical wall at the calving front. This is a deviation from the  
 312 real system, but an acceptable one, since our focus lies on processes inside the glacier  
 313 cavity, which are not much affected by this difference.

### 314 **2.2.2 Surface friction**

315 Where the ocean is covered by glacier ice, there is a no-slip boundary condition at  
 316 the sea surface (Burchard et al., 2022). This friction at the ice–ocean interface is imple-  
 317 mented in GETM according to the law-of-the-wall with a roughness length  $z_{0,\text{ice}}$ , simi-  
 318 lar to bottom friction. In our default scenario, we use the value  $z_{0,\text{ice}} = 0.01$  m. The  
 319 effects of smoother or rougher ice are tested in our sensitivity analysis (Section 3.3.5).

### 2.2.3 Parametrization of subglacial melting

We implemented the subglacial melt formulation by Burchard et al. (2022). This parametrization, based on the three-equation model (D. M. Holland & Jenkins, 1999), is suitable for high vertical resolutions under the ice. In our free-surface model, meltwater is added like precipitation as a real freshwater flux (Huang, 1993) to the uppermost grid cell of the water column with a melt rate  $v_b$  (in  $\text{m s}^{-1}$ ). There is no salt flux,  $f_b^S = 0$ , because the melted glacier ice is assumed to have zero salinity. There is, however, a temperature flux at the ice–ocean interface:

$$f_b^T = v_b \left[ \frac{c_i}{c} (\theta_b - T_i) + \frac{L_i}{c} - \theta_b \right]. \quad (2)$$

In the squared bracket, the first term corresponds to the energy necessary for heating up the glacial ice from its core temperature  $T_i$  to the melt layer temperature  $\theta_b$ ; the second term is the latent heat of the phase change from ice to water; the last term appears because water is exchanged between ice and ocean, *i.e.*, the ice–ocean interface is a non-material interface in our model (Jenkins et al., 2001). The values of the constants in (2) are given in Table 1. The melt layer is a thin layer at the ice–ocean interface, that is not resolved but parametrized in our model. For a detailed discussion, see Burchard et al. (2022).

The here-described implementation of melting differs from that used by Burchard et al. (2022), because their 1D model has a rigid lid. In a rigid lid model, the water volume cannot increase, so a virtual salt flux through the ice–ocean interface is needed to get the diluting effect of basal melting on salinity, and a virtual temperature flux is needed instead of (2). However, the more realistic approach is adding meltwater explicitly (Huang, 1993; Jenkins et al., 2001), without a salt flux and with only a real temperature flux, as we do it in this study. Even though melting increases the water volume in our model, the ice volume does not decrease. To allow for a decreasing ice volume and a thinning ice tongue, ice dynamics would have to be modeled as well. Instead, we assume that there is a balance between basal melting of the ice tongue and the discharge of glacier ice from land into the ocean.

### 2.3 Adaptive vertical coordinates

Our GETM setup uses adaptive vertical coordinates (AVC) described by Burchard and Beckers (2004) and Hofmeister et al. (2010). These coordinates are well-suited for representing surface-attached buoyant plumes (Chegini et al., 2020) and dense bottom currents (Hofmeister et al., 2010; Umlauf et al., 2010). AVC are topography-following coordinates, in which the vertical distribution of the model layers changes with time. The temporal change of model layers is implemented by minimizing a cost function depending on the model state, particularly the stratification. The coordinates adapt in a way that there are more layers in parts of the water column with higher stratification. This ensures high vertical resolution in areas of strong vertical density gradients and minimizes numerical mixing (Hofmeister et al., 2010; Klingbeil et al., 2014; Gräwe et al., 2015).

In the 79NG fjord, important density differences exist in two locations: (i) Between the meltwater plume at the ice–ocean interface and the ambient water below, and (ii) between the bottom current and the cavity water above (Schaffer et al., 2020). With AVC we can obtain high resolutions in both of these plumes and particularly in their entrainment layers, without a large increase in computational cost ( $< 10\%$  more computation time compared to  $\sigma$ -coordinates). For this, we configured AVC so that they zoom towards stratification and towards the sea surface. An explicit bottom-zooming is not required, because the stratification-zooming itself provides sufficiently high resolution in the bottom plume (Section 3.2). Activating the zooming towards the sea floor would also result in high resolution in the deep trough of the glacier fjord and on the continental shelf outside the ice cavity, even though these parts are mostly inactive in our simulations.

370 Thus, we do not activate it and opt instead for an even higher resolutions near the ice–  
 371 ocean interface, which is important for the accurate representation of melting (Burchard  
 372 et al., 2022). While 50 coordinate levels would be sufficient to achieve a vertical reso-  
 373 lution better than 2 m in the plume under the ice, we present in this paper simulations  
 374 with 100 AVC layers to show the plumes and the circulation in great detail.

## 375 2.4 Analysis of plume-averaged quantities

376 To analyze the entrainment of the subglacial plume, we compute its bulk proper-  
 377 ties, *i.e.*, the vertically averaged plume characteristic, in particular the plume thickness,  
 378  $D$ , its buoyancy  $\bar{b}$ , and its velocity  $\bar{u}$ . We want to diagnose the bulk values following the  
 379 ideas by Arneborg et al. (2007) in the modified form for plumes under ice shelves (Burchard  
 380 et al., 2022):

$$381 \quad \bar{b}D = \int_{-\infty}^{\eta} b(z) dz, \quad (3)$$

$$382 \quad \bar{b}D^2 = 2 \int_{-\infty}^{\eta} b(z)z' dz, \quad (4)$$

$$383 \quad \bar{u}D = \int_{-\infty}^{\eta} u(z) dz, \quad (5)$$

384 where  $z' = \eta - z$  is the distance from the ice–ocean interface,  $b(z) = -g[\rho(z) - \rho_0]/\rho_0$   
 385 is the buoyancy, and  $\rho_0$  is the ambient ocean density. However, the above equations have  
 386 been derived in a 1D setting with the assumptions that the ambient water below the plume  
 387 is homogeneous (with density  $\rho_0$ ) and stagnant ( $u = 0$ ), which is not the case in our  
 388 2D model. So an integration to  $-\infty$  or to the sea floor at  $z = -H$  would not make sense,  
 389 because it would include several different water masses in the plume analysis. Instead,  
 390 we choose an integration depth  $h_0 > 0$ , consider the water mass at  $z = \eta - h_0$  as the  
 391 ambient water, and use the following modified formulas

$$392 \quad \bar{b}D = \int_{\eta-h_0}^{\eta} b(z) dz, \quad (6)$$

$$393 \quad \bar{b}D^2 = 2 \int_{\eta-h_0}^{\eta} b(z)z' dz, \quad (7)$$

$$394 \quad \bar{u}\bar{b}D = \int_{\eta-h_0}^{\eta} u(z)b(z) dz, \quad (8)$$

395 as definitions of plume thickness  $D$ , plume buoyancy  $\bar{b}$ , and plume velocity  $\bar{u}$ . Note that  
 396 dividing (7) by (6) gives  $D$ , dividing (8) by (6) gives  $\bar{u}$ , and dividing (6) by  $D$  gives  $\bar{b}$ .  
 397 We take as  $\rho_0$  the density linearly interpolated from cell centers to  $z = \eta - h_0$ ; a ver-  
 398 tical interpolation gives considerably smoother graphs for the bulk values than taking  
 399 the density of the grid cell containing  $z = \eta - h_0$ . The factors of  $b(z)$  and  $\bar{b}$  in (8) en-  
 400 sure that the integral gives more weight inside the plume than outside, where  $b(z)$  is smaller  
 401 since the local density  $\rho(z)$  is closer to that of the ambient water,  $\rho_0$ . We use velocities  
 402 horizontally interpolated to cell centers (instead of cell interfaces) in (8), so that all bulk  
 403 values are defined on cell centers.

404 Following P. R. Holland and Feltham (2006), the bulk values can be used to for-  
 405 mulate a conservation equation for the plume volume:

$$406 \quad \partial_t D + \partial_x(D\bar{u}) + \partial_y(D\bar{v}) = v_b + v_e, \quad (9)$$

407 where the terms on the right-hand side are the melt rate  $v_b$  and the entrainment veloc-  
 408 ity  $v_e$ . For our 2D system ( $\partial_y = 0$ ) in steady state ( $\partial_t = 0$ ), (9) implies

$$409 \quad \bar{u}\partial_x D = -D\partial_x \bar{u} + v_b + v_e, \quad (10)$$

410 which means that the plume thickness increases in  $x$ -direction by flow convergence ( $-D\partial_x\bar{u}$ ),  
 411 melting, and entrainment (Jenkins, 1991). Since the melting is computed by our numer-  
 412 ical model, we can reformulate (10) to diagnose the entrainment (Burchard et al., 2022):

$$413 \quad v_e = D\partial_x\bar{u} + \bar{u}\partial_x D - v_b. \quad (11)$$

414 To further analyze the dynamics of the plume, we compute the Froude number

$$415 \quad \text{Fr} = \frac{|\bar{u}|}{\sqrt{|b|D}}, \quad (12)$$

416 which is a non-dimensional number relating the velocity of the plume to the phase speed  
 417 of long waves at the plume interface (Arneborg et al., 2007; Burchard et al., 2022). In  
 418 flows that are dominated by a balance between buoyancy and friction, with little accel-  
 419 eration, the approximation

$$420 \quad \text{Fr} \approx \sqrt{\frac{\tan \alpha}{c_d}} \quad (13)$$

421 holds (Arneborg et al., 2007), where  $\tan \alpha = \partial\eta/\partial x$  is the slope of the topography and

$$422 \quad c_d = \left[ \frac{\kappa}{\ln \left( \frac{\frac{1}{2}D + z_{0,\text{ice}}}{z_{0,\text{ice}}} \right)} \right]^2 \quad (14)$$

423 is the drag coefficient of the subglacial plume (Burchard et al., 2022) with the van Kar-  
 424 man constant  $\kappa = 0.4$ .

425 The choice of the integration depth  $h_0$  requires some considerations. It must be cho-  
 426 sen such that (as long as the plume is attached to the ice)  $z = \eta - h_0$  lies always out-  
 427 side the plume in a weakly stratified region, but not too far away, so that  $\rho_0 = \rho(z =$   
 428  $\eta - h_0)$  is actually the density of the water surrounding the plume. To find a suitable  
 429 integration depth, a visual inspection of the model result is helpful. The identified value  
 430 is a good choice if the computed bulk values are insensitive to small variations of  $h_0$ . In  
 431 our default scenario, this is the case for  $h_0 = 10$  m. However, the precise choice of  $h_0$   
 432 is not critical for the results.

433 For the analysis of the dense bottom plume, we use an analogous approach, but  
 434 with integration from the sea floor at  $z = -H$  to  $z = -H + h_0$ , and with  $z' = H +$   
 435  $z$  being the distance from the sea floor in (7). As integration height  $h_0$ , we take  $h_0 =$   
 436  $30$  m downstream of the sill and  $h_0 = h_0(x) = 30 \text{ m} + H(x) - H(x_{\text{sill}})$  upstream of  
 437 the sill, where  $x_{\text{sill}} = 80$  km is the position and  $H(x_{\text{sill}}) = 300$  m the depth of the sill.  
 438 This way, on the upstream side of the sill, the integration goes from the sea floor to a  
 439 constant level of  $z = -270$  m, which is the depth that separates the inflowing water mass  
 440 below from the outflowing water mass above. Like for the subglacial plume, the precise  
 441 choice of  $h_0$  is not critical.

## 442 2.5 Analysis of the overturning circulation

443 A key property of a glacier fjord is the strength of its overturning circulation, of-  
 444 ten reported in milli-Sverdrup ( $1 \text{ mSv} = 1000 \text{ m}^3 \text{ s}^{-1}$ ). We take as a measure of the over-  
 445 turning strength the maximum (in absolute value) of the (volume) stream function over  
 446 the sill ( $x = 80$  km). This value is smaller than the overall maximum of the stream func-  
 447 tion, which is reached in the interior of the cavity, but it allows the comparison of our  
 448 results with measurements near the calving front (Schaffer et al., 2020). Since the over-  
 449 turning in the cavity is stronger than over the sill, the term *exchange flow* might be more  
 450 suitable than *overturning strength*, but we use the latter for consistency with the liter-  
 451 ature. The stream function  $\psi$  is defined by

$$452 \quad \partial_z \psi = uL_y, \quad (15)$$

$$453 \quad \partial_x \psi = -wL_y, \quad (16)$$

454 and the condition that  $\psi = 0$  on the sea floor;  $L_y$  is the (constant) width of the fjord  
 455 (Table 1). Numerically, we diagnose  $\psi$  by summing the horizontal transports  $u\Delta zL_y$  (de-  
 456 fined on cell edges) from the sea floor to the sea surface, which follows from (15) and nat-  
 457 urally satisfies  $\psi = 0$  at the bottom. Then (16) is automatically fulfilled thanks to the  
 458 2D continuity equation,  $\partial_x u + \partial_z w = 0$ . Since the model results shown in this paper  
 459 are in steady state, the contour lines of the stream function  $\psi$  are trajectories.

### 460 3 Results

461 In this section, we present at first the steady state of our default scenario (Sections 3.1  
 462 and 3.2), then we perform a sensitivity study with varying physical parameters (Section 3.3).

#### 463 3.1 Circulation and melting in the default scenario

464 In our default model setup, which is an idealized representation of the present day  
 465 situation at 79NG as observed by Schaffer et al. (2020), we find an estuarine-like circu-  
 466 lation in the glacier cavity (Fig. 3a–d). This circulation is made up of two gravity plumes:  
 467 strong, turbulent, and focused currents that are driven by density differences. One is a  
 468 buoyant plume at the lower ice edge, driving the melting of the ice tongue and transport-  
 469 ing glacially modified water out of the fjord into the ambient ocean (blue in Fig. 3a). The  
 470 other plume – a dense bottom current – brings warm and salty Atlantic Intermediate  
 471 Water (AIW) from the open ocean over the sill into the glacier cavity (red in Fig. 3a).  
 472 The strength of the overturning circulation is 39 mSv (Fig. 3b), consistent with the value  
 473 of  $(46 \pm 11)$  mSv obtained from hydrographic measurements (Schaffer et al., 2020).

474 Subglacial melting creates a layer of cold water just below the ice along the whole  
 475 glacier tongue (Fig. 3c). This meltwater is transported away from the glacier and intro-  
 476 duces a layer of cold water into the ambient ocean at depths of around 90 m to 95 m be-  
 477 low sea level. Minimum temperatures offshore the calving front are below  $-1.5^\circ\text{C}$  at 94 m  
 478 depth. Apart from this layer and its immediate surroundings, the temperature strati-  
 479 fication offshore the sill is mostly in equilibrium with the imposed open ocean conditions.  
 480 As the flow of AIW from the open ocean into the glacier cavity is hindered by the sill,  
 481 the cavity water becomes colder than the open ocean water by mixing with meltwater  
 482 (inset of Fig. 3c).

483 Salinity differences are the main drivers of the circulation in the 79NG fjord (Fig. 3d).  
 484 On the one side, the subglacial plume rises along the ice tongue because it is fresher, thus  
 485 lighter than the water inside the cavity. On the other side, AIW flows down the bottom  
 486 slope into the glacier cavity because it is saltier, thus denser than the cavity water. Com-  
 487 paring the water at the same depth on both sides of the sill, we see that the cavity wa-  
 488 ter, which is a mixture of AIW with meltwater, is at least  $0.1\text{ g kg}^{-1}$  fresher than AIW  
 489 (inset of Fig. 3d). Offshore the sill, the salinity stratification is almost horizontally ho-  
 490 mogeneous and in equilibrium with the imposed conditions of the open ocean.

491 Along the whole ice tongue of 79NG, the basal melt rate is positive, *i.e.*, no freez-  
 492 ing appears in our simulation (Fig. 3e). We find the strongest melting of  $58\text{ m yr}^{-1}$  close  
 493 to the grounding line and a mostly monotonic decrease of the melt rate afterwards. The  
 494 melt rate reaches practically zero ( $< 0.1\text{ m yr}^{-1}$ ) at around 42 km from the grounding  
 495 line. The rest of the ice tongue has an average melt rate of less than  $0.01\text{ m yr}^{-1}$ . The  
 496 position where the melting stops is the place where the subglacial plume detaches from  
 497 the ice tongue (see Section 3.1.1). The melt rate averaged over the whole ice tongue is  
 498  $12.3\text{ m yr}^{-1}$  (corresponding to  $20.3\text{ km}^3\text{ yr}^{-1}$ ) in our model, consistent with the value of  
 499  $(10.4 \pm 3.1)\text{ m yr}^{-1}$ , or  $(17.8 \pm 5.2)\text{ km}^3\text{ yr}^{-1}$ , estimated by Schaffer et al. (2020) based  
 500 on measurements. Accordingly, also the percentage of subglacial discharge in the total  
 501 meltwater production at 79NG is similar between our model (9.8%) and observations

**Circulation, Temperature, Salinity, and Melting in the 79° North Glacier Fjord**

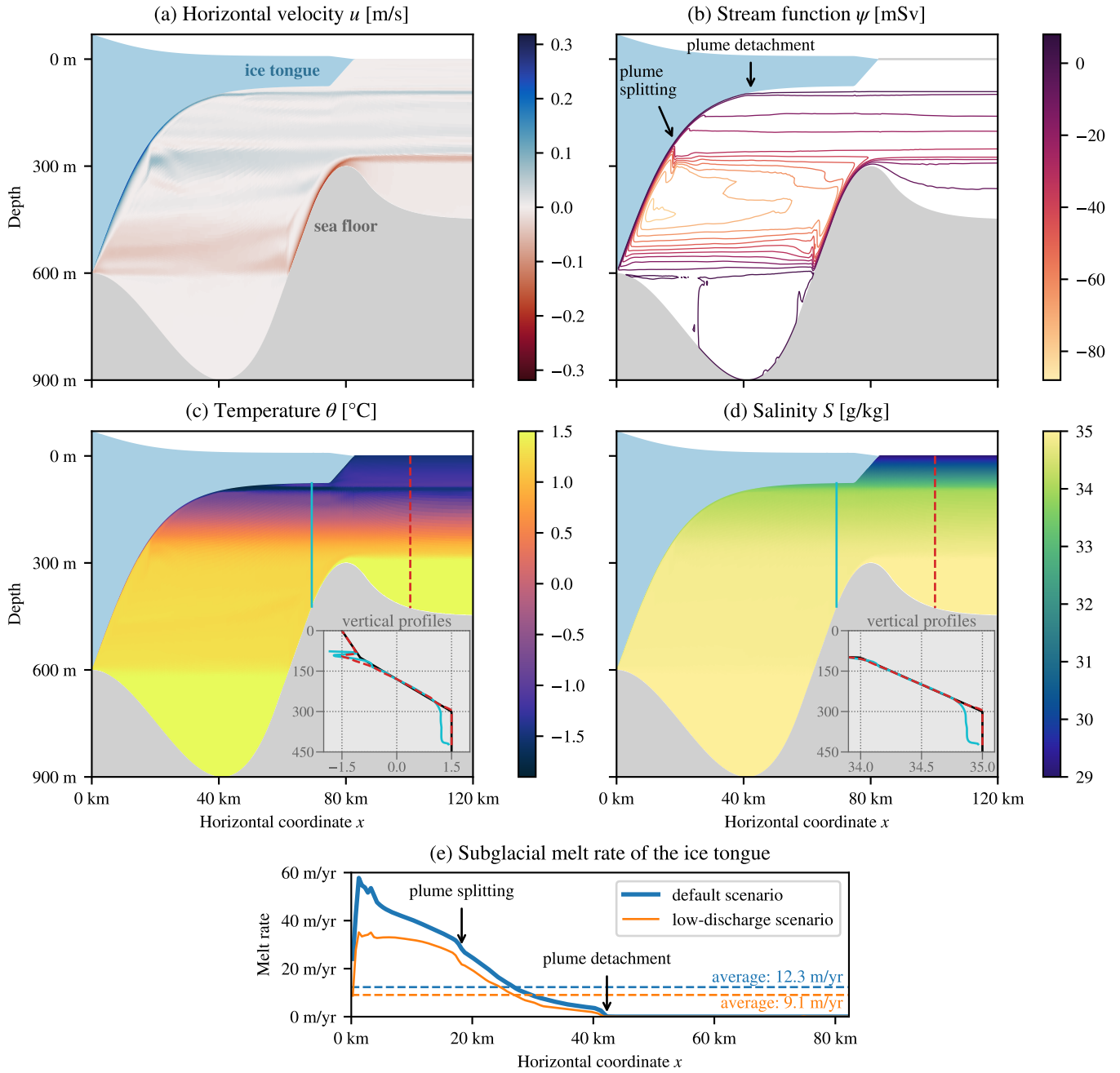


**Figure 3.** Model results in steady state for our default scenario of the 79NG fjord showing horizontal velocity (a), stream function (b), temperature (c), salinity (d), and melt rate (e). Insets in panels (c) and (d) show vertical profiles of temperature and salinity, respectively, at positions on both sides of the sill marked with vertical lines in the same colors as the graphs; conditions at the open boundary are shown in black for comparison. The thin orange line in panel (e) corresponds to a sensitivity experiment, in which the subglacial discharge is reduced by an order of magnitude compared to the default scenario (Section 3.3.3).

502 (11%; Schaffer et al., 2020). This shows that basal melting is by far the dominant fresh-  
 503 water source in the glacier fjord.

### 504 **3.1.1 The buoyant subglacial plume**

505 The subglacial plume starts at the grounding line ( $x = 0$ ), where subglacial runoff  
 506 is discharged into the cavity. Since this discharge is fresher than the water in the fjord,  
 507 it is positively buoyant and rises along the lower ice edge. We observe in our model that  
 508 two opposing processes modify the plume water while rising. On its upper side, the plume  
 509 causes melting of the ice tongue due to the turbulent heat flux, parameterized as a func-  
 510 tion of the friction velocity, which adds cold and fresh meltwater to the plume. On its  
 511 lower side, ambient water is entrained upwards into the plume by turbulent mixing, thus  
 512 making it saltier and warmer. This way, entrainment transports heat towards the ice and  
 513 amplifies the melting (Jenkins, 2011; Burchard et al., 2022). As the plume rises, it passes  
 514 through ever lighter surrounding water and reaches a point where its density equals that  
 515 of the ambient water (Fig. 4a). This is between 95 m and 100 m below sea level. At this  
 516 level, the subglacial plume detaches from the ice tongue, propagates horizontally away  
 517 from the glacier, and transports glacially modified water out of the fjord (Fig. 3a-c). This  
 518 observation is qualitatively consistent with the plume detachment and cold-water export  
 519 at mid-depth in the model of an Antarctic ice shelf by Hellmer and Olbers (1989).

520 Before its detachment, the plume splits up a number of times. The first splitting  
 521 occurs at 18 km from the grounding line (Fig. 5). Until there, the plume was rising through  
 522 well-mixed water, allowing it to grow and thicken rapidly by entrainment. However, around  
 523 the depth of the sill (300 m), the ambient water changes from almost unstratified to sta-  
 524 bly stratified (Fig. 5d). The lower part of the plume consisting of denser water that has  
 525 been advected with the buoyant melt water overshoots its neutral level. It falls about  
 526 70 m down, rises slightly again, and finds its neutral level near  $z = -290$  m, where it  
 527 propagates away from the ice (Fig. 5a,b). This creates a buoyancy oscillation visible in  
 528 the streamlines (Fig. 3b). However, the oscillation is strongly damped, because the plume  
 529 mixes with ambient water during its ascent and descent (Fig. 5c), thereby reaching neu-  
 530 tral buoyancy quickly (Fig. 5d). Similar though smaller splits of the plume can be ob-  
 531 served several times until the plume detachment. This creates a vertical velocity pro-  
 532 file with a number of velocity peaks between the depth of the calving front and the depth  
 533 of the sill (Fig. 3a). A similar velocity profile has been observed in reality. Velocity mea-  
 534 surements at the calving front of 79NG show the main outflow of glacially modified wa-  
 535 ter near 100 m depth, in addition to weaker outflows at greater depths (Schaffer et al.  
 536 2020). These deeper outflows may be caused by the splitting of the subglacial plume.

538 Prior to the splitting of the plume, its thickness increases from  $D = 3$  m at a dis-  
 539 tance of 5 km from the grounding line to about  $D = 5$  m at  $x = 18$  km (Fig. 4a). Over  
 540 this distance, the plume becomes more buoyant and increases its vertically-averaged ve-  
 541 locity  $\bar{u}$  to a maximum of  $0.22 \text{ m s}^{-1}$  (Fig. 4b,c). When the plume splits, its velocity drops  
 542 and so does its buoyancy  $\bar{b}$ , because the ambient water below the plume becomes lighter.  
 543 After the splitting, the plume thickens more slowly and reaches  $D = 6$  m at  $x = 40$  km,  
 544 just before its detachment from the ice. When it detaches, the plume buoyancy drops  
 545 again (Fig. 4c), meaning that the plume density is similar to the ambient density, which  
 546 is the reason for the plume detachment. Note that the buoyancy does not go to zero be-  
 547 cause the formulas to compute  $\bar{b}$  (Section 2.4) are only applicable while the plume is within  
 548 10 m from the ice edge; afterwards, the thin lines in Fig. 4b-d represent the properties  
 549 of the water just below the ice.

550 Entrainment at the plume base is only positive until the plume splits for the first  
 551 time (Fig. 6a). The plume thickening afterwards is mainly due to flow convergence (Fig. 6a)  
 552 in consequence of the plume slowing down (Fig. 4b). It is not due to entrainment, be-

**Details of the Subglacial Plume (a–d) and of the Bottom Plume (e–h)**

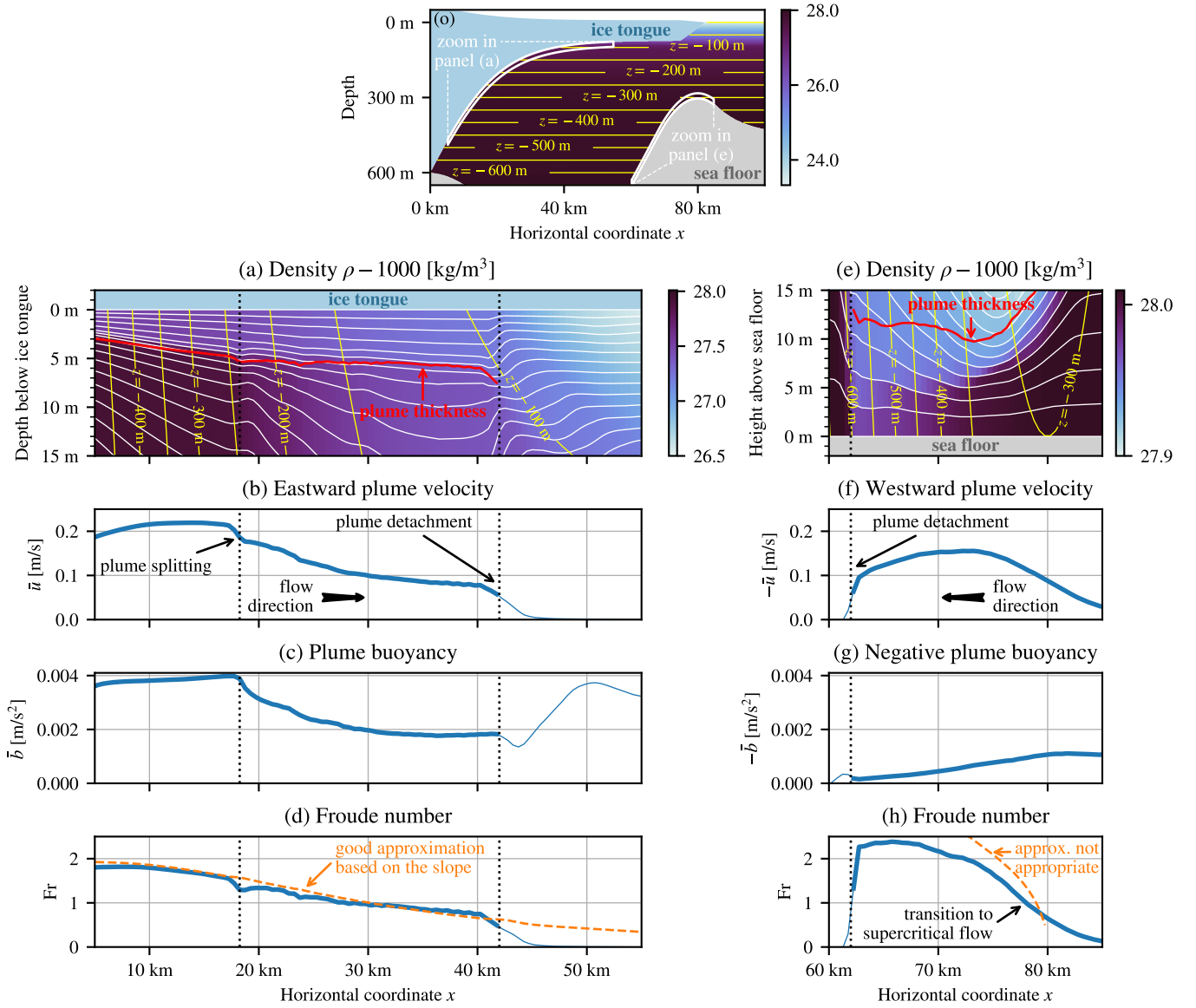


**Figure 4.** Details of the buoyant plume (a–d) and of the dense plume (e–h) in the default scenario. Panels (a) and (e) show density in the 15 m just below the ice tongue and in the 15 m just above the sea floor, respectively. The shown areas are marked in white in the overview panel (o). Note the different starting points of the colorbars. White lines in (a) and (e) are coordinate levels (upper/lower cell edges of the model grid) and emphasize the high vertical resolution of about 1 m obtained by AVC in the entrainment layers of both plumes. The red lines represent the thicknesses  $D$  of the plumes before their detachments, which are marked by dotted vertical lines. After its detachment, the water of the subglacial plume in (a) flows horizontally in parallel to the yellow  $z = -100$  m isobath. Note that the bulk values in panels (f) and (g) have opposite signs than those in (b) and (c), because the plumes go in opposite directions and are oppositely buoyant. After the plume detachments, bulk values are shown as thin lines, because they do not represent the plumes anymore, but are averages of the uppermost 10 m under the ice (b–d) or the lowermost 30 m above the sea floor (f–h), see Section 2.4 for details. Panels (d) and (h) show the Froude numbers (solid) computed by (12) in addition to their approximations (dashed) computed by (13).

**Zoom to the first splitting of the subglacial plume**

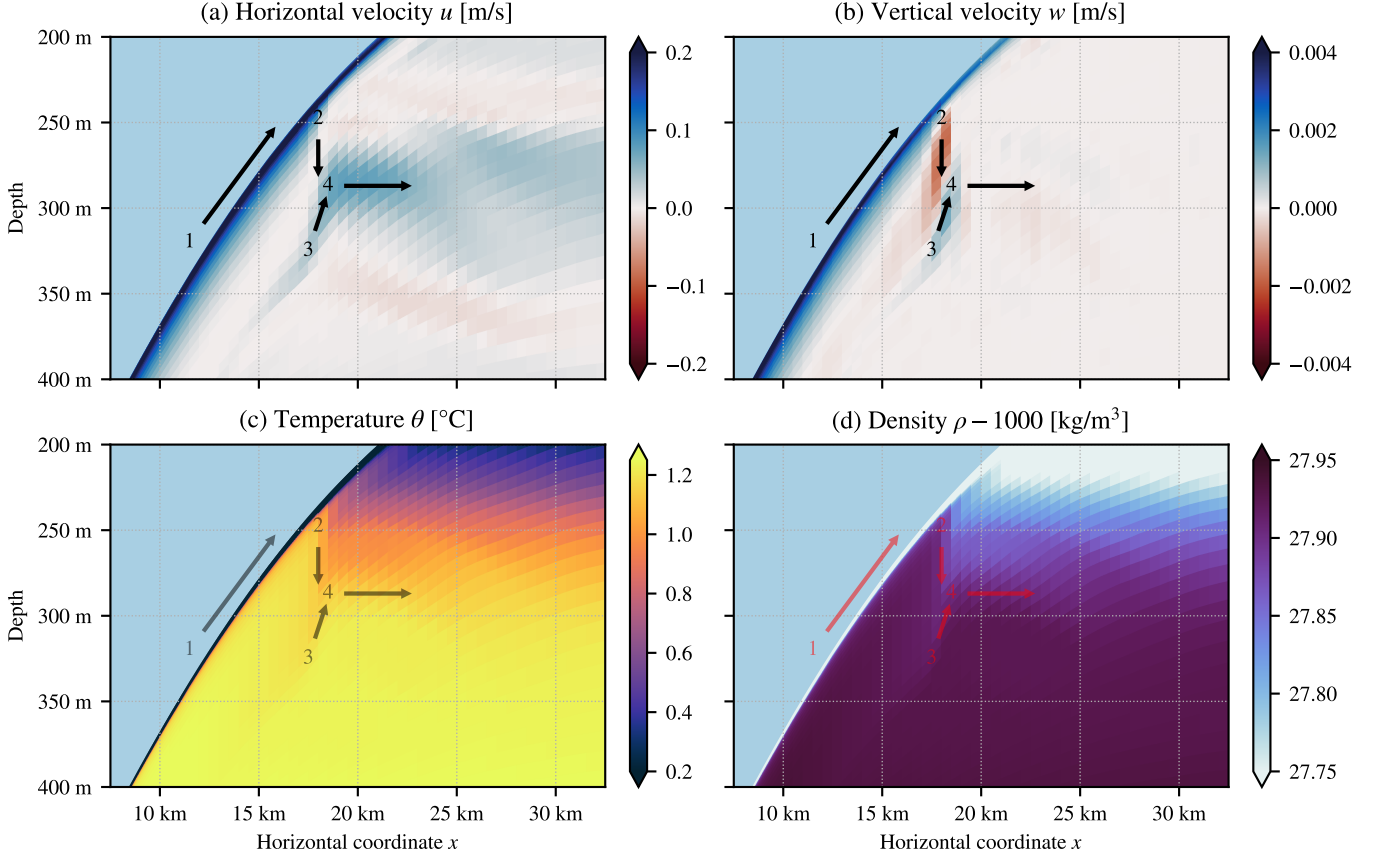


**Figure 5.** Zoom to the first splitting of the subglacial plume (default scenario). The arrows represent the flow direction resulting from the combined effects of the horizontal (a) and vertical (b) velocity components: (1) The plume rises along the ice tongue; (2) the lower part of the plume falls down from about 250 m depth to about 320 m depth, while becoming slightly colder and lighter due to mixing with ambient water; (3) the plume rises to about 290 m depth and (4) flows horizontally away from the ice tongue.

553 cause after the initial phase, the entrainment velocity  $v_e$  is negative and detrainment ap-  
 554 pears (Fig. 6a). So instead of taking up ambient water, the plume in total loses water  
 555 to the stratified interior of the cavity (Fig. 3). Correspondingly, the vertical velocity un-  
 556 der the plume is negative, *i.e.*, downward (Fig. 6c). The detrained water forms an out-  
 557 flowing layer below the plume (Fig. 6b).

558 Our interpretation of the detrainment is that initially, the weakly stratified water  
 559 in the deep part of the cavity allows strong turbulence to develop (Fig. 6d), leading to  
 560 high entrainment rates of  $E = v_e/\bar{u} = \mathcal{O}(2 \times 10^{-4})$  and rapid plume thickening (Fig. 4a),  
 561 consistent with the initial plume development and entrainment reported by Burchard  
 562 et al. (2022). When the plume arrives in the more stratified upper part of the cavity, the  
 563 reduced turbulence is insufficient to sustain the thick plume. Comparing turbulent kin-  
 564 etic energy (TKE) in the entrainment part with the detrainment part, we see that in  
 565 the latter case, TKE is clearly reduced at the ice–ocean interface, at the plume base, and  
 566 below the plume (Fig. 6d). So the turbulence might be too weak to further entrain am-

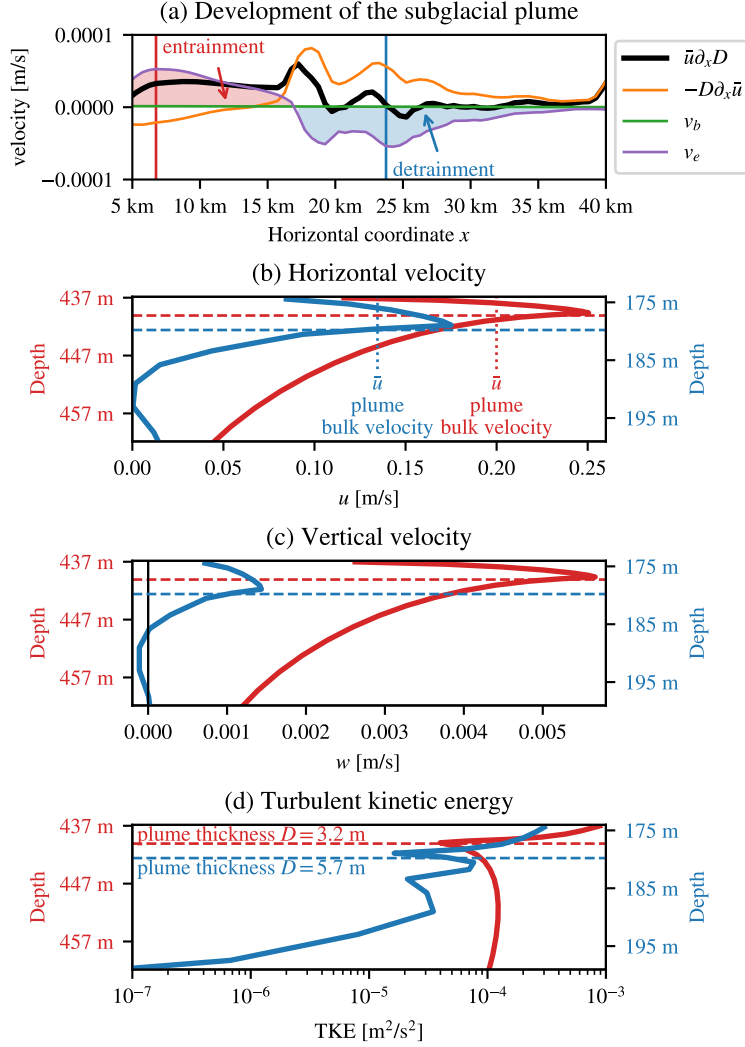


**Figure 6.** Development of the subglacial plume thickness  $D$  before the detachment from the ice tongue, with areas of entrainment and detrainment highlighted (a); vertical profiles at positions near maximum entrainment (red) and detrainment (blue), showing velocity components (b,c) and turbulent kinetic energy (d) in the 25 m under the ice (default scenario). The colored graphs in (a) represent the processes acting on the plume thickness: flow convergence (orange), subglacial melt rate (green, close to zero), and entrainment velocity at the plume base (purple); summed together, they give the thicker black line, see (10). For the calculation of the graphs in (a), plume thickness  $D$  and bulk velocity  $\bar{u}$  were smoothed with a running average of window size  $\pm 1$  km.

567 bient water against gravity, and instead the plume detrains water. This manifests in the  
 568 first plume splitting near  $x = 18$  km and the subsequent smaller splits as described above.

569 The Froude number,  $Fr$ , of the subglacial plume (eq. 12) is very close to its approx-  
 570 imation (eq. 13) based on the ice slope and the drag coefficient (Fig. 4d). This indicates  
 571 that the plume is dominated by friction at the ice–ocean interface (Arneborg et al., 2007),  
 572 which is plausible, as the plume is a rather thin boundary layer. The decreasing Froude  
 573 number can thus be considered a consequence of the decreasing ice slope. Since the plume  
 574 dynamics are determined by friction, there seems to be no hydraulic jump at the posi-  
 575 tion where  $Fr = 1$ . This is different for the dense bottom plume discussed in the next  
 576 subsection.

### 577 **3.1.2 The dense bottom plume**

578 The bottom plume in the 79NG fjord consists of AIW coming from the open ocean.  
 579 With a density of  $1028.0 \text{ kg m}^{-3}$  (Fig. 4e), this is the densest water mass in our system,  
 580 as well as the warmest and saltiest (Fig. 3c,d). It flows from the sill at  $x = 80$  km down  
 581 into the cavity, following the bathymetry. As long as the bottom slope increases, the plume  
 582 accelerates up to a vertically-averaged velocity of  $\bar{u} = -0.16 \text{ m s}^{-1}$  (Fig. 4f). Due to  
 583 this flow divergence, the plume thins from 17 m over the sill to 10 m thickness six kilo-  
 584 meter downstream (Fig. 4e). The rapid plume thinning is associated with a transition  
 585 from subcritical flow ( $Fr < 1$ ) in the plume before it passes the sill to supercritical flow  
 586 ( $Fr > 1$ ) as the plume flows down the slope (Fig. 4h). Just downstream of the sill, the  
 587 Froude number becomes equal to one, which means that the sill acts as a hydraulic control  
 588 for the bottom plume and limits the inflow of AIW into the cavity. This is consis-  
 589 tent with hydrographic measurements around the sill at 79NG, which also indicated hy-  
 590 draulic control (Schaffer et al., 2020).

591 While flowing down the bottom slope, the plume entrains ambient cavity water,  
 592 which has a lower density since it contains meltwater (Fig. 4e). In consequence, the plume  
 593 density and buoyancy (in absolute value) decrease (Fig. 4g). Similar to the subglacial  
 594 plume, the bottom plume transports water below its neutral depth. The water then rises  
 595 again and adjusts in an oscillating way to its level of neutral buoyancy (Fig. 3b), before  
 596 propagating horizontally away from the bathymetry. This way, the bottom plume fills  
 597 the cavity with (partially mixed) AIW over a depth range of 450 m to 600 m (Fig. 3a).  
 598 At about 600 m below sea level, the plume has detached completely from the bottom.  
 599 It cannot propagate further down, because the entrainment of cavity water made the plume  
 600 lighter than the water in the trough below 600 m depth. The water in the deep trough  
 601 is dense because it consists of almost pure AIW (from the initialization) with only lit-  
 602 tle meltwater. This is because (i) meltwater enters the cavity only at depths where the  
 603 ice tongue is present, and (ii) the meltwater is not mixed far below the grounding line  
 604 (600 m) due to the absence of strong motion there.

605 Outside the cavity, just offshore the sill, even some AIW below the sill level moves  
 606 upward and flows over the sill (Fig. 3b). This overflow is driven by an internal pressure  
 607 gradient that is vertically homogeneous, since the water on the upstream side of the sill  
 608 is unstratified. The phenomenon of upward acceleration of dense water against gravity  
 609 is called aspiration and commonly observed in fjords (Inall & Gillibrand, 2010).

### 610 **3.2 Performance of the adaptive vertical coordinates (AVC)**

611 AVC is one feature of our model that has not been employed before in simulations  
 612 of glacier fjords. Our setup uses 100 vertical layers that adapt automatically to the strat-  
 613 ification, as explained in Section 2.3. This way, we reach high vertical resolutions in both  
 614 plumes.

615 The vertical resolution in the subglacial plume is everywhere close to 1 m and even  
 616 better in the entrainment layer at the plume base (white lines in Fig. 4a). Thus, AVC  
 617 achieve the necessary resolution to represent the entrainment into and detrainment out  
 618 of the plume correctly (Burchard et al., 2022). Since the model layers adapt to and fol-  
 619 low the plume, its water is advected mostly along the layers and not across. The plume  
 620 is always resolved by five layers or more while it is attached to the ice, which allows pre-  
 621 serving the plume properties well. Models with  $z$ -coordinates usually do not achieve this,  
 622 which causes the plume to spread out. For example, the layer of cold water under the  
 623 ice is around 50 m thick in the 2D model of Hellmer and Olbers (1989), much more than  
 624 the 5 m-thin plume in our setup. This shows an important advantage of stratification-  
 625 zooming coordinates.

626 When the plume splits (Fig. 5) and when it detaches from the ice (Fig. 4a), AVC  
 627 also attempt to follow the flow of the meltwater by partially bending in the horizontal  
 628 direction, but cannot follow the plume as well as when it is at the ice. In consequence,  
 629 the plume must pass through layers that are not fully aligned with its flow direction, in-  
 630 creasing the numerical diffusion. The calving front presents another challenge for AVC.  
 631 As terrain-following coordinates, they must connect the lower ice edge to the sea level,  
 632 a difference of 75 m in depth. However, the flow under the calving front is horizontal and  
 633 the density is horizontally homogeneous, so there is necessarily a divergence between co-  
 634 ordinates and plume. By stretching the calving front over 7.5 km as explained in Sec-  
 635 tion 2.2.1, the vertical position of the ice–ocean interface changes gradually enough, so  
 636 that the coordinates manage to adapt to the plume to some extent and preserve its prop-  
 637 erties well (see the inset of Fig. 3c). However, a slight dilution of the plume as it passes  
 638 under the calving front and through several layers can still be seen (Fig. 3a–c).

639 Similar to the subglacial plume, also the incoming plume of Atlantic Water is re-  
 640 solved by several layers with a thickness on the order of 1 m (Fig. 4e). As the plume prop-  
 641 agates down the slope, it thins due to velocity divergence, so the number of layers in the  
 642 plume reduces.

643 The high resolution in the vicinity of the ice and the bottom comes at the expense  
 644 of thicker layers in the interior of the glacier cavity. While the vertical layers are less than  
 645 10 m thick in most areas, there are up to 15 m-thick layers in the middle of the water col-  
 646 umn in places where the fjord is deepest. However, we believe that this is a good trade-  
 647 off, because (i) the thick layers appear in areas where the velocities are small and the  
 648 water column is only weakly stratified, and (ii) we obtain very thin layers in the dynam-  
 649 ically relevant parts.

### 650 3.3 Sensitivity studies

651 We now explore how the results change compared to the default scenario for mod-  
 652 ified environmental influences. Key properties of all presented scenarios are summarized  
 653 in Table 2.

#### 654 3.3.1 Influence of the ambient ocean salinity

655 The subglacial plume detaches from the ice tongue and transports meltwater out  
 656 of the fjord towards the open ocean at a depth of around 95 m below sea level in our de-  
 657 fault scenario. This sensitivity study shows that the depth depends strongly on the salin-  
 658 ity stratification of the ambient ocean, which is imposed at the open boundary of the  
 659 model. When the salinity of the upper water column is increased, the plume propagates  
 660 further along the ice tongue and detaches higher up. With lower salinities above the sill,  
 661 the plume does not propagate as far up and detaches earlier.

662 This relation is exemplified by the two sensitivity experiments shown in Fig. 7 in  
 663 comparison with the default case. For the high salinity scenario, we increased the sur-

**Table 2.** Summary of the presented simulations

Scenario	Melt rate ( $\text{m yr}^{-1}$ )	Overturning (mSv)	Runoff
default	12.3	39.2	9.8%
high salinity	12.6	40.1	9.6%
low salinity	10.2	32.2	11.6%
AIW: $-1.0$ K	7.6	35.1	15.0%
AIW: $-0.5$ K	10.0	39.0	11.8%
AIW: $+0.5$ K	15.5	43.8	8.0%
AIW: $+1.0$ K	19.0	47.7	6.6%
PW: $+0.5$ K	12.3	39.3	9.9%
PW: $+1.0$ K	12.2	38.9	9.9%
AIW & PW: $+0.5$ K	15.3	42.0	8.0%
AIW & PW: $+1.0$ K	18.7	47.1	6.7%
discharge 1/10-th	9.1	25.7	1.5%
discharge doubled	14.3	49.9	15.8%
sill at 200 m	9.2	21.7	12.7%
sill at 250 m	11.1	31.2	10.7%
sill at 350 m	13.2	57.1	9.2%
sill at 400 m	13.3	78.1	9.1%
no sill	13.4	107.2	9.1%
smooth ice (z0m)	16.1	52.5	7.7%
rough ice (z0p)	5.6	30.8	19.4%
Observation	$10.4 \pm 3.1$	$46 \pm 11$	11%

Melt rate is the subglacial melt rate averaged over the whole ice tongue. Overturning is the strength of the circulation measured above the sill. Runoff is the percentage of subglacial discharge in the total meltwater outflow (discharge plus melting) of the fjord. Observation cites the values reported by Schaffer et al. (2020). AIW stands for (the temperature of) Atlantic Intermediate Water, PW for Polar Water.

664 face salinity from  $29 \text{ g kg}^{-1}$  to  $33.5 \text{ g kg}^{-1}$ , so that we obtain a linear salinity stratifica-  
665 tion in the upper 300 m of the water column (Fig. 7b). With this stratification, the plume  
666 detaches at around 50 m below sea level (Fig. 7a). In the low salinity case, we kept the  
667 surface value at  $29 \text{ g kg}^{-1}$  but decreased the salinity at 100 m depth from  $34 \text{ g kg}^{-1}$  to  
668  $33.5 \text{ g kg}^{-1}$  (Fig. 7f). Then most of the plume detaches between 125 m and 150 m of depth  
669 (Fig. 7e). These experiments also show that the plume detachment is not caused by the  
670 abruptly changing stratification that is in the default scenario at a similar depth as the  
671 detachment (Fig. 7c,d).

672 In fact, it is the salinity of the open ocean that determines the depth where the plume  
673 detaches. The salinity at the detachment level is  $(33.7 \pm 0.1) \text{ g kg}^{-1}$  in all three scenar-  
674 ios. We also tested a stratification with a minimum salinity of  $34 \text{ g kg}^{-1}$  (not shown),  
675 in which case the plume never detaches from the ice tongue but reaches sea level. The  
676 reason that the detachment depth depends strongly on salinity is that at this level, the  
677 plume density equals that of the ambient ocean, which is set primarily by salinity in the  
678 79NG fjord.

679 For the deeper half of the ice tongue, the plume developments and melt rates are  
680 basically identical between our sensitivity experiments, but they differ in the upper 300 m.  
681 At the plume detachments, the subglacial melt rates drop to almost zero, which shows  
682 again that the subglacial plume is responsible for the bulk of basal melting. In the sce-

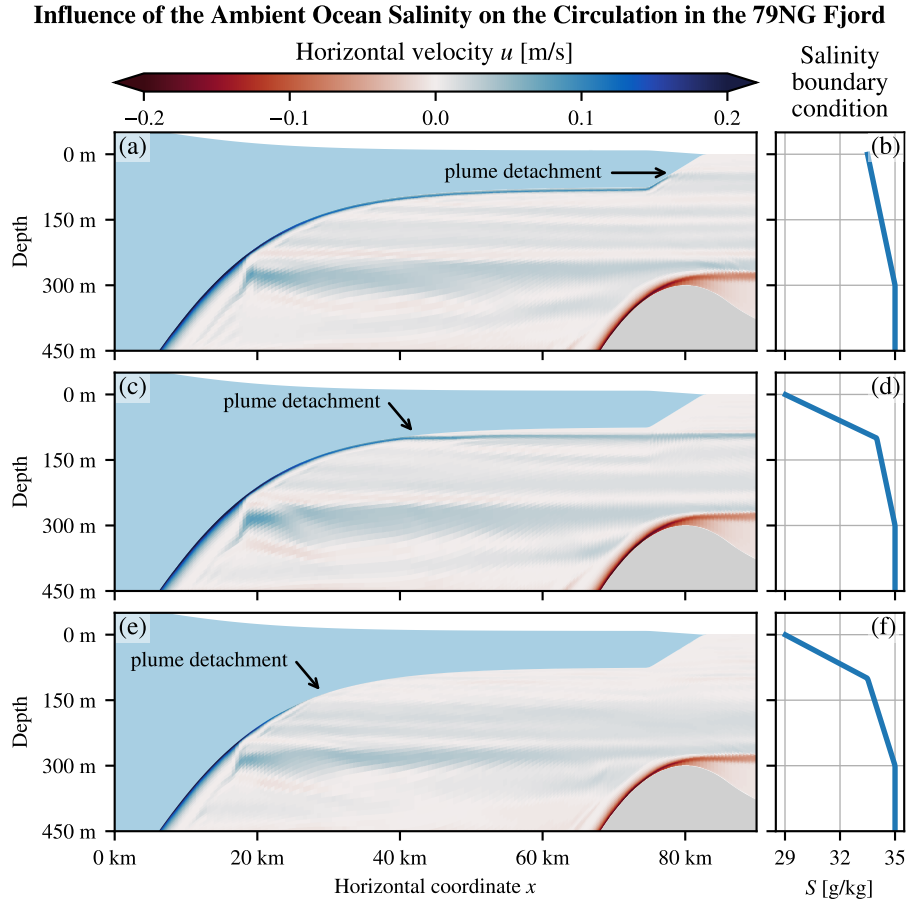


**Figure 7.** Experiments on the sensitivity of 79NG to the open ocean stratification, with higher salinity (a,b) than in our default scenario (c,d) as well as lower salinity (e,f). For higher salinities above the sill, the subglacial plume propagates further along the ice tongue and detaches higher up. The salinity at the level of plume detachment is always around  $33.7 \text{ g kg}^{-1}$ . When the plume detaches early (e), a weaker secondary plume develops above.

683 nario with the plume detachment at great depths, a small second plume develops above  
 684 the main detachment, causing some more melting with melt rates up to  $0.7 \text{ m yr}^{-1}$  be-  
 685 fore detaching near 100 m depth (Fig. 7e). Only in the scenario with a late plume de-  
 686 tachment, we observe melt rates above  $0.2 \text{ m yr}^{-1}$  along the whole ice tongue up to the  
 687 calving front. However, note that the plume development as it propagates up the calv-  
 688 ing front in this scenario (Fig. 7a) is not entirely realistic, because the calving front is  
 689 sloping in our model and not vertical (Section 2.2.1).

### 690 **3.3.2 Influence of the ambient ocean temperature**

691 We investigate the influence of the imposed temperature stratification at the open  
 692 ocean boundary by varying the temperatures of Polar Water (PW) and Atlantic Inter-  
 693 mediate Water (AIW) individually as well as together. In our model, PW occupies the  
 694 upper 100 m of the water column and has in the default scenario a linear temperature  
 695 profile with  $-1.5 \text{ }^\circ\text{C}$  at sea level and  $-1.0 \text{ }^\circ\text{C}$  at 100 m depth (Fig. 2b). AIW fills the wa-  
 696 ter column below 300 m depth and has a vertically homogeneous temperature of  $1.5 \text{ }^\circ\text{C}$   
 697 by default. In between 100 m and 300 m, we apply a linear temperature gradient. In our

698 sensitivity study, we increase the temperatures of AIW and/or PW by 0.5 K or 1.0 K.  
 699 We also decrease AIW temperatures by 0.5 K and 1.0 K. Note that we cannot make PW  
 700 colder, because the surface temperature is just above freezing in our default scenario (Fig. 2b).

701 We observe that the AIW temperature has a clearly larger impact on the glacier  
 702 cavity than variations of PW temperature. With increasing AIW temperature, the sub-  
 703 glacial melt rate increases along the whole ice tongue (Table 2) and the point at which  
 704 the plume detaches moves upward. For AIW temperatures of 0.5 °C, the plume detaches  
 705 below 130 m, for 2.5 °C above 90 m depth. This can be explained by the increased tem-  
 706 perature forcing, which causes more melting and thereby a lighter plume that rises faster  
 707 and further. Interestingly, in the deep part of the cavity, the thickness of the subglacial  
 708 plume is not much altered by temperature differences, although this is the part where  
 709 AIW is present.

710 Our findings are qualitatively consistent with modeling studies of the circulation  
 711 under Antarctic ice shelves. Hellmer and Olbers (1989) reported a plume detachment  
 712 at greater depth and a reduced overturning circulation when the inflowing bottom wa-  
 713 ter has a lower temperature, and the opposite effect for a higher temperature. Even though  
 714 they also modified the inflowing salinity in addition to the temperature, they claimed  
 715 that the observed effects are actually due to the temperature variation, which is confirmed  
 716 by our results. Grosfeld and Gerdes (1998) observed that increased temperatures of the  
 717 water flowing into the cavity led to strongly increased melting, which reduces the salin-  
 718 ity of the outflow. This fits with our observations of a lighter plume that detaches later  
 719 from the ice tongue, at a depth where the salinity is lower.

720 The parametrization by Slater and Straneo (2022) captures the temperature de-  
 721 pendence of the melt rate well, but only in the vicinity of the grounding line. Let us first  
 722 consider the 15 km of the ice tongue directly after the grounding line, which is the part  
 723 where the plume rises through a water mass that is similar to AIW (Fig. 3c,d). In this  
 724 area, the average melt rate computed in our simulations is best described by  $(8 \pm 1)(\Delta\theta)^{1.24 \pm 0.09}$ ,  
 725 where  $\Delta\theta$  is the temperature forcing, *i.e.*, the difference between AIW temperature and  
 726 the freezing point at the grounding line. The values after  $\pm$  are 95 %-confidence inter-  
 727 vals, so our fit is consistent with the  $(\Delta\theta)^{1.19}$ -proportionality used by Slater and Stra-  
 728 neo (2022), though with a larger constant of proportionality. However, if we average over  
 729 the full length of the ice tongue, the melt rate can be parameterized as  $(1.3 \pm 0.2)(\Delta\theta)^{1.69 \pm 0.09}$ .  
 730 The exponent is significantly larger, but smaller than in the  $(\Delta\theta)^2$ -law found by Holland  
 731 et al. (2008). This shows that a close-to linear relation between melting and thermal forc-  
 732 ing is only applicable near the grounding line (Slater & Straneo, 2022) and should not  
 733 be applied to the whole ice tongue. A linear relation between melt rate and  $\Delta\theta$  was sug-  
 734 gested by Jenkins (2011) and Xu et al. (2012), which fits with our modeled melt rates  
 735 up to about 4 km from the grounding line.

736 The effects associated with increased PW temperatures are much smaller. Cavity  
 737 circulation and both plumes look practically the same as in the default scenario. The  
 738 only (small) difference we observe is in the detachment point of the subglacial plume.  
 739 It moves about 2 m down for a PW temperature increase of 0.5 K and about 3 m (com-  
 740 pared to default) for a 1.0 K-increase. This makes sense because the upper part of the  
 741 water column is lighter for warmer PW, so the plume reaches its neutral buoyancy ear-  
 742 lier. Since subglacial melting almost stops when the plume detaches, the overall melt rate  
 743 is slightly lower for higher PW temperatures (Table 2). However, note that our model  
 744 does not simulate calving, which can be intensified in warmer water.

745 When we increase the temperatures of both AIW and PW together, thus making  
 746 the whole water column warmer, we observe a combination of the effects described above.  
 747 The results look similar to those with only increased AIW temperatures, but the sub-  
 748 glacial plume detaches at a slightly deeper level.

749

### 3.3.3 Role of the subglacial discharge

750

751

752

753

754

755

756

757

758

759

760

761

762

The meltwater discharged at the grounding line has an important influence on subglacial melting. In our default scenario, we prescribe a constant subglacial discharge of  $70 \text{ m}^3 \text{ s}^{-1}$ , which is the value reported by a field campaign (Schaffer et al., 2020), and we find a clear, peaked melt rate maximum just after the grounding line. In contrast, if we reduce the discharged water volume in our model by an order of magnitude to  $7 \text{ m}^3 \text{ s}^{-1}$ , we observe a flatter melt distribution after the grounding line with a lower and rather constant melt rate over the first 10 km (Fig. 3e). Interestingly, after the splitting of the subglacial plume, the melt distributions look similar for low discharge and normal discharge (Fig. 3e). Also, the position of the plume detachment from the ice tongue is not much different. These observations suggest that the subglacial discharge has mostly an impact on the early development of the plume (consistent with Jenkins, 2011), while further away from the grounding line, the plume development is mostly determined by subglacial melting and the ambient ocean stratification.

763

764

765

766

767

768

Due to the decreased subglacial melting in scenarios with lower subglacial discharge, the cavity water is warmer, saltier, and denser. This has the effect that the dense bottom plume does not propagate as far down the slope and detaches earlier from the bottom. Also, both plumes are thinner and slower than in the default scenario. The strength of the overturning circulation is reduced by about one third to 26 mSv for a discharge of  $7 \text{ m}^3 \text{ s}^{-1}$  (Table 2).

769

770

771

772

773

We observe the opposite effects when we increase the subglacial discharge: The melt rate increases; the cavity water becomes colder, fresher, and lighter; the plumes are thicker and faster. Doubling the discharge to  $140 \text{ m}^3 \text{ s}^{-1}$  increases the overturning strength by about one fourth (relative to default scenario) to 50 mSv and the average melt rate by about one sixth to  $14.3 \text{ m yr}^{-1}$  (Table 2).

774

775

776

777

778

779

780

781

The relation between subglacial discharge  $Q$  and average subglacial melt rate  $\langle v_b \rangle$  in our system does not properly follow the commonly reported  $\langle v_b \rangle \propto Q^{1/3}$ -law (Fig. 8; Jenkins, 2011; Xu et al., 2012; Slater & Straneo, 2022). Only if we restrict the averaging  $\langle \cdot \rangle$  to the first 1 km of the ice tongue, we find that the melt rate is proportional to  $Q^{0.27 \pm 0.04}$  (not shown). This fit would include, in its 95 %-confidence interval, the  $Q^{0.31}$ -proportionality used by Slater and Straneo (2022) and is also close to the  $Q^{1/3}$ -law suggested by Jenkins (2011) and Xu et al. (2012). But the average contains just two grid cells and is thus not representative of the whole ice tongue.

782

783

784

785

786

787

788

789

790

791

792

793

794

795

Considering the melt rate averaged over the full ice length, the best fit to our model data is  $\langle v_b \rangle = (6.4 \pm 0.6) Q^{0.16 \pm 0.02}$ , suggesting that the melt rate is roughly proportional to  $Q^{1/6}$  (Fig. 8). However, such a law would imply a zero melt rate for zero discharge, which is not plausible as plumes develop also under ice shelves without subglacial discharge. For example at 79NG, mooring data indicate a year-round outflowing plume, even in the months without subglacial discharge (Lindeman et al., 2020; Schaffer et al., 2020). To allow for plume-induced melting in the absence of subglacial discharge, we fit the function  $\langle v_b \rangle = cQ^e + d$  to seven model runs with different values of  $Q$ . A least-squares regression gives the coefficient  $c = 0.8 \pm 0.3$ , the offset  $d = 7.2 \pm 0.5$ , and the exponent  $e = 0.44 \pm 0.06$  (values after  $\pm$  are 95 %-confidence intervals). The fit clearly describes our model results better than the  $Q^{1/3}$ -law and also slightly better than the  $Q^{1/6}$ -law (Fig. 8). This means that in the absence of subglacial discharge, the average melt rate is about  $7 \text{ m yr}^{-1}$ , and increases approximately with the square root of the subglacial discharge,  $\sqrt{Q}$ .

796

797

798

799

In our model, we cannot reasonably increase the subglacial discharge arbitrarily. For example, with a discharge of  $700 \text{ m}^3 \text{ s}^{-1}$  (ten-times the default), the large amount of meltwater leaving the cavity cannot be transported across the open boundary, because the prescribed conditions at the open boundary correspond to the default scenario, which

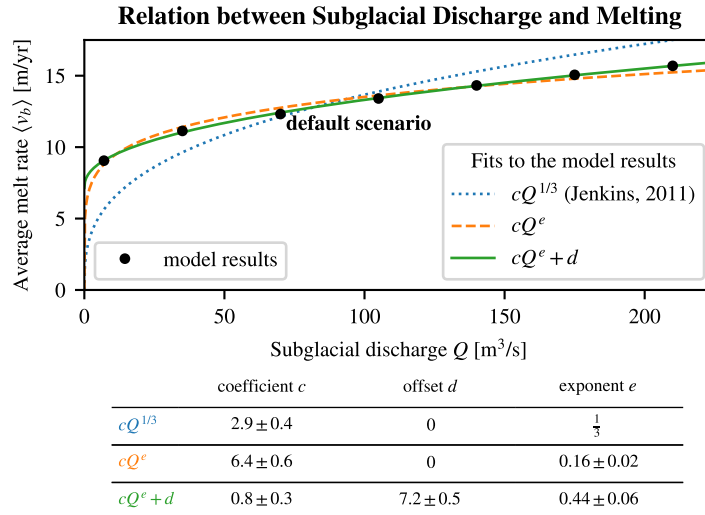


**Figure 8.** Subglacial melt rate averaged over the whole ice tongue,  $\langle v_b \rangle$ , in the default model run and six sensitivity experiments with varying subglacial discharge,  $Q$ , (black circles) compared to three simple parametrizations (colored graphs). The  $Q^{1/3}$ -law proposed by Jenkins (2011) does not give a good fit (dotted, blue). The parametrization proportional to  $Q^{0.31}$  used by Slater and Straneo (2022) is very similar to the  $Q^{1/3}$ -law (not shown). A better fit is obtained by using an exponent of  $0.16 \pm 0.02$ , which is roughly a  $Q^{1/6}$ -law (dashed, orange). The best fit is obtained by allowing a non-zero melt rate for zero subglacial discharge, which is close to a  $\sqrt{Q}$  law that is shifted upward by about  $7 \text{ m yr}^{-1}$  (solid, green).

800 has lower discharge and melting. This causes a density front near the open boundary,  
 801 which is physically unstable and prevents the system from reaching a steady state. Nev-  
 802 ertheless, the model stays numerically stable, even in such a non-equilibrium situation.

### 803 3.3.4 Role of the sill

804 Our model allows us to test a hypothesis made by Schaffer et al. (2020) based on  
 805 their hydrographic measurements. They claim that the bathymetry of the 79NG fjord  
 806 constrains the heat transport from the open Atlantic ocean into the glacier cavity. Ac-  
 807 cording to Schaffer et al. (2020), the height of the sill at the fjord entrance determines  
 808 how much warm AIW flows into the fjord, and in turn how much heat is available for  
 809 subglacial melting. In our idealized 2D model, we can easily modify the sill height (de-  
 810 fault: 300 m below sea level) or remove the sill completely and check which impact it has.

811 We find that the cavity water is clearly colder with a higher sill than with a lower  
 812 sill or without a sill (Fig. 9a,b, see also Fig. 3c). The higher the sill, the stronger the tem-  
 813 perature contrast between the water in the cavity and the water on the continental shelf.  
 814 Consequently, the melt rate is larger if the sill is at greater depths and *vice versa* (Fig. 9c,d).  
 815 Interestingly, the melt rate is not larger over the full length of the ice tongue, but mostly  
 816 in the  $(20 \pm 5)$  km after the grounding line, where the ice is at great depths. The melt-  
 817 ing of the thinner part of the ice tongue is not much influenced by the sill, neither is the  
 818 position of the plume detachment from the ice. When the sill is at 350 m below sea level  
 819 or deeper, the melt rate is almost independent of the sill depth (Fig. 9c,d). At this depth,  
 820 the sill cannot effectively prevent the warm AIW from entering the cavity anymore.

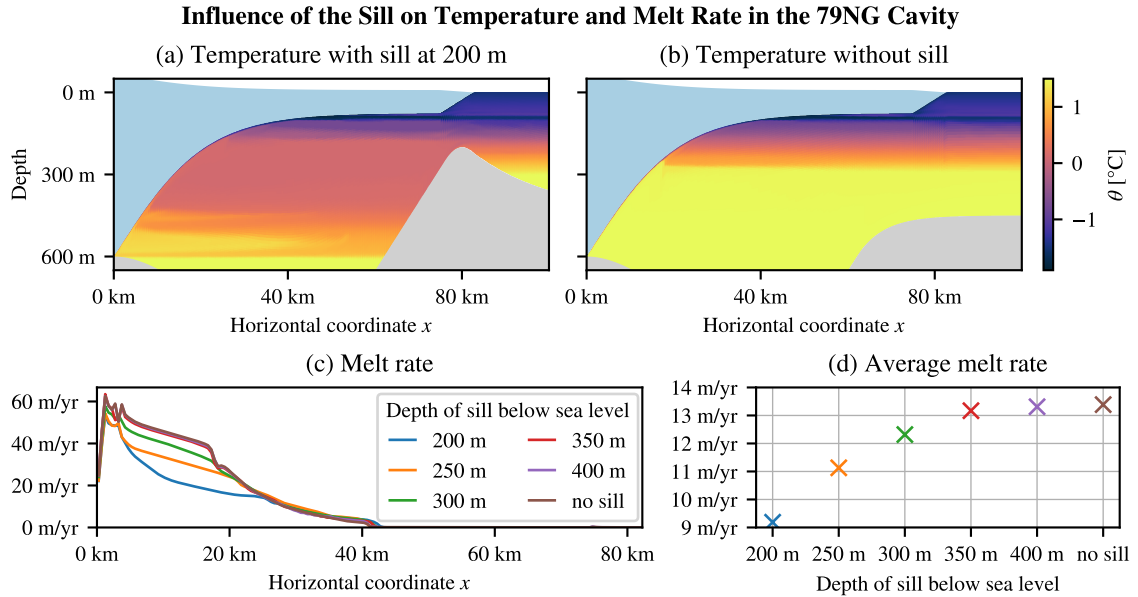


**Figure 9.** Temperature in the glacier cavity in a modified 79NG fjord with a high sill (a) and with no sill (b), as well as subglacial melt rate of the 79NG ice tongue with  $x$ -resolution (c) and in spatial average (d) for different sill depths (including no sill). When the sill is higher, *i.e.*, with a lower sill depth, less warm water can flow into the cavity, so the melt rate is lower. Note that the continental shelf offshore the cavity is at 450 m below sea level, so a sill depth of 450 m means no sill.

821 So our simulations show that indeed the sill height constrains the heat transport  
 822 into the cavity and thereby determines the melt rate of the 79NG ice tongue. This “sill  
 823 effect” almost ends at a depth of about 350 m, measured from sea level.

### 824 3.3.5 Roughness length

825 In our setup, the smoothness or roughness of the ice tongue on its underside is mod-  
 826 eled by a roughness length,  $z_{0,ice}$ . This parameter has the value 0.01 m in our default sce-  
 827 nario, but it is poorly known which value is realistic for a given ice shelf (P. R. Holland  
 828 & Feltham, 2006; Jourdain et al., 2017). To test the sensitivity of the 79NG system on  
 829 this value, we increased the roughness length by a factor of ten ( $z_{0,ice} = 0.1$  m, scenario  
 830 z0p) and decreased it by a factor of ten ( $z_{0,ice} = 0.001$  m, scenario z0m). We also tested  
 831 intermediate values to ensure that our observations are actually tendencies as reported  
 832 below.

833 Our model results show that the shorter the roughness length, the larger the melt  
 834 rate and the stronger the overturning circulation (Table 2). Due to the higher melting,  
 835 the subglacial plume becomes colder (Fig. 10c,d), fresher, and more buoyant. It accel-  
 836 erates faster and has a higher velocity under the ice and after its detachment (Fig. 10a,b).  
 837 Also the inflowing bottom plume is faster with a shorter ice roughness length (not shown),  
 838 contributing to the increased overturning strength (Table 2). In the scenario with rougher  
 839 ice (z0p), most of the plume detaches from the ice tongue already at a depth of 200 m  
 840 and leaves the fjord at this level, while the outflow at 100 m-depth is much weaker (Fig. 10b,d).  
 841 Initially, the plume thickens quickly by entrainment, but detains strongly from 16 km  
 842 to 24 km behind the grounding line, leading to an almost complete detachment of the  
 843 plume at around 24 km from the grounding line (Fig. 10b). Behind this point, the plume

844 is thinner than in the other two scenarios. In the scenario with smoother ice ( $z_{0m}$ ), the  
 845 plume is everywhere thinner than in the default scenario.

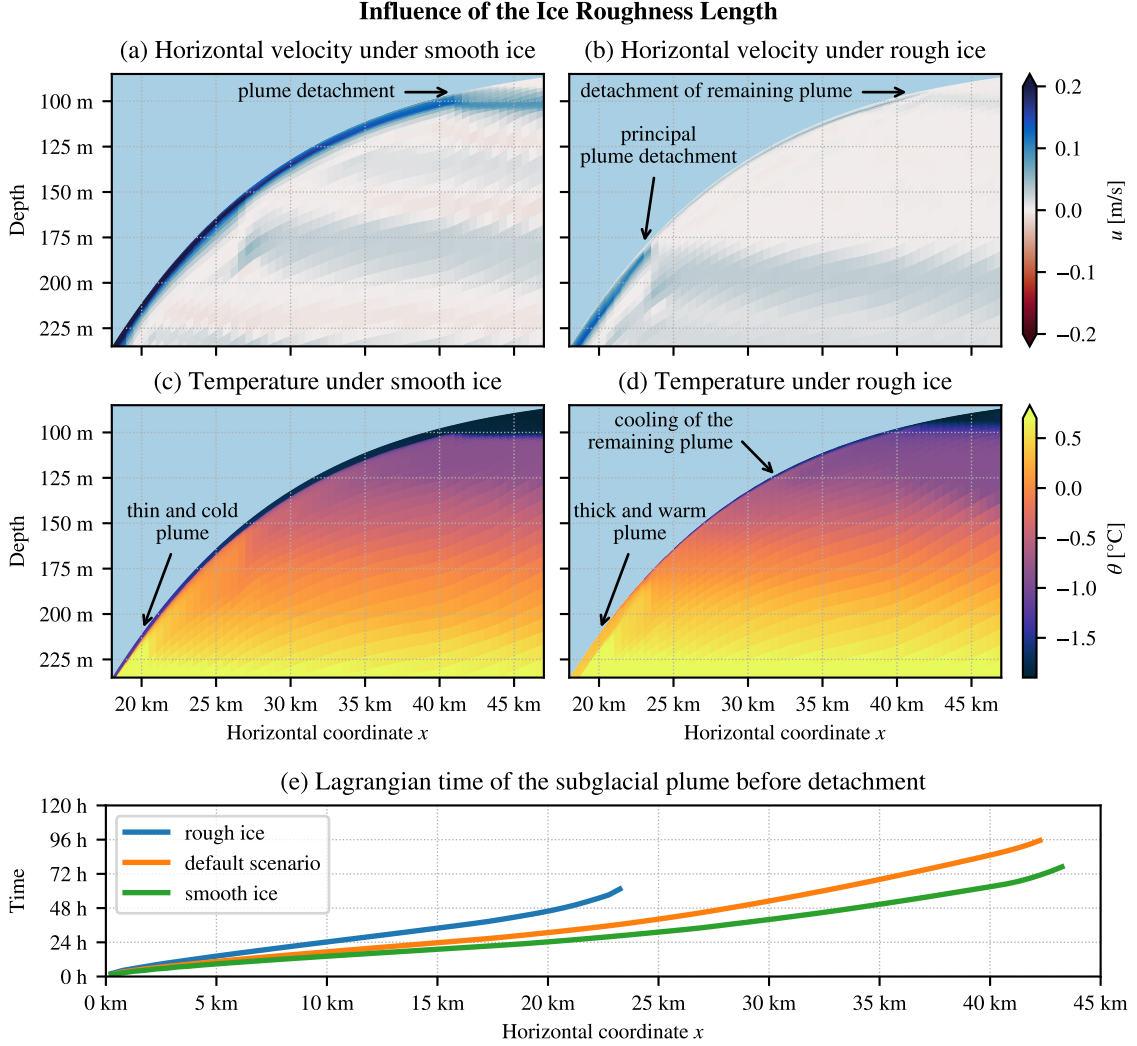


**Figure 10.** Influence of the roughness length of the ice tongue,  $z_{0,ice}$ , on the circulation (a,b) and the temperature (c,d) below the ice tongue as well as on the Lagrangian time of the subglacial plume (e). The Lagrangian time  $t$ , defined as the integral of  $dt = dx/\bar{u}$ , is shown up to the (principal) plume detachment, see panels (a), (b), and Fig. 3; this position is identified by a clear reduction of under-ice velocity  $u$  and plume velocity  $\bar{u}$ .

846 The reasons for the observed effects of varying ice roughness are complex. The tur-  
 847 bulent heat transfer velocity  $\gamma_T$  in the melt formulation depends on the ice roughness  
 848 length  $z_{0,ice}$  (Burchard et al., 2022). Lower roughness leads to higher heat transfer, which  
 849 can explain the higher melt rate. In consequence of the increased melting, the subglacial  
 850 plume becomes more buoyant, which means that the density difference between plume  
 851 and ambient water is larger. The stronger stratification at the plume interface hinders  
 852 entrainment, and this lower entrainment in turn leads to a stronger stratification, possi-  
 853 bly indicating a positive-feedback loop. This loop eventually breaks as the plume rises  
 854 along the ice, because the lighter plume accelerates faster and reaches higher velocities,  
 855 which then increase turbulent mixing and entrainment. The divergence caused by the

856 strong initial acceleration together with the initially weak entrainment explain why the  
857 plume under smoother ice is thinner.

858 Consistent with our findings, also Jenkins (1991) reported higher melting in exper-  
859 iments with a lower drag coefficient, which corresponds to a shorter roughness length.  
860 The model used by Jenkins (1991) is a 1D plume model that – like our model – does not  
861 take into account the impact of Earth rotation. Models that include Coriolis show ad-  
862 ditional effects in response to increased ice roughness. In a realistic setup of the Amund-  
863 sen Sea, Jourdain et al. (2017) varied the drag and the heat transfer independently of  
864 each other. They found that melting increases with the heat exchange coefficient  $\Gamma_T$ , with  
865 the drag coefficient  $c_d$ , and also with the Stanton number  $St = \sqrt{c_d}\Gamma_T$  (Jourdain et al.,  
866 2017). This does not conflict with our results, because heat transfer and drag are not  
867 independent in our model. For smoother ice, the drag coefficient is lower, but the heat  
868 exchange is higher, in a way that the Stanton number is generally larger. So, the higher  
869 heat transfer compensates for the lower drag and results in stronger melting at smoother  
870 ice. However, Earth rotation also deflects the plume away from the direction of the steep-  
871 est ascent. This effect is stronger, the lower the friction at the ice–ocean interface (P.  
872 R. Holland & Feltham, 2006). A plume under smooth ice may be deflected until it is at  
873 the side wall of the fjord, where wall drag slows down the plume, which then leads to  
874 lower melting (P. R. Holland & Feltham, 2006). This makes the consequences of vary-  
875 ing ice roughness more complex (Payne et al., 2007). However, the model by P. R. Hol-  
876 land and Feltham (2006), which was also employed by Payne et al. (2007), cannot rep-  
877 resent the plume detachment. The same is true for the water column model of a sub-  
878 glacial plume by Burchard et al. (2022), which they applied to a setting similar to 79NG.  
879 They found that in the initial phase of the plume development, the melt rate is higher  
880 for smoother ice, while in a later phase, the relation is reversed. The transition from the  
881 initial to the later phase occurs after about one week (Burchard et al., 2022). Our model  
882 shows that the plume detaches from the ice always within one week. In a Lagrangian sense,  
883 the plume needs less than four days to reach the point at which it detaches from the ice,  
884 in all analyzed scenarios (Fig. 10e). Thus, the plume at 79NG goes only through the ini-  
885 tial phase. Models without plume detachment might also simulate the later phase, which  
886 does not always occur, as shown by our results for 79NG. This can lead to different con-  
887 clusions regarding the relation between drag at the ice–ocean interface and subglacial  
888 melting.

## 889 4 Discussion

890 In large-scale ocean models without explicitly resolved glacier cavities, meltwater  
891 from fjords is often introduced at the sea surface (e.g., Stolzenberger et al., 2022). Our  
892 model results show that this is generally not realistic for fjords with an ice tongue. This  
893 matches with a similar observation from a high-resolution model of a fjord with a ver-  
894 tical glacier front (Xu et al., 2013). In our default scenario, the bulk of meltwater leaves  
895 the 79NG fjord between 90 m and 100 m below sea level (Section 3.1 and Fig. 3a–c). This  
896 level depends primarily on the stratification of the ambient ocean, which is mainly set  
897 by salinity. Even a relatively small change in the upper ocean salinity can alter the out-  
898 flow depth of glacially modified water by 50 m (Section 3.3.1 and Fig. 7). The temper-  
899 ature stratification also influences the outflow depth, but less dramatically, as our sen-  
900 sitivity study shows (Section 3.3.2). On the other hand, the outflow depth is almost un-  
901 affected by the subglacial discharge and by the sill at the fjord entrance, despite their  
902 big influence on subglacial melting and overturning circulation in the cavity (Sections 3.3.3  
903 and 3.3.4). If the base of the ice tongue had a higher roughness, the outflow around 95 m  
904 depth would be weaker but still at the same depth as for smooth ice (Section 3.3.5 and  
905 Fig. 10a,b). We suspect that the outflow depth of meltwater does not change much with  
906 seasons, because the fjord properties that have a strong seasonality are the subglacial  
907 runoff (Lindeman et al., 2020; Schaffer et al., 2020) and the ocean surface temperature,

908 which both have little impact on the outflow level. Whether the sub-surface stratifica-  
 909 tion at 79NG, which is important for the outflow depth, shows seasonal variability, is still  
 910 unknown, but the existing mooring data shows no clear signature of a seasonal cycle (Lindeman  
 911 et al., 2020; Schaffer et al., 2020, and own analysis of their datasets). Longer time series  
 912 of measurements at 79NG are necessary to answer this question.

913 Our analysis of entrainment rates (Fig. 6) reveals that the dynamics of the sub-  
 914 glacial plume at 79NG fall into two different regimes. The first one is analogue to the  
 915 so-called plume regime (Baines, 2008). This is the case over the first 17 km from the ground-  
 916 ing line, where the ice slope is high and the ambient stratification is low. The plume shows  
 917 strong entrainment, partly overshoots its density horizon, falls down again, and intrudes  
 918 over a wide range of depths (Fig. 5). However, at 17 km from the grounding line, the en-  
 919 trainment rate switches sign (Fig. 6a). The boundary layer leaves the plume regime and  
 920 enters that of a gravity current. The gravity current, which exists under a more gently  
 921 sloping ice, is characterized by detrainment, *i.e.*, it loses water to the stratified interior  
 922 of the cavity (Baines, 2008). When the gravity current finds its neutral density level af-  
 923 ter around 40 km from the grounding line, it detaches from the ice tongue without over-  
 924 shooting (Fig. 3). Both behaviors of the turbulent boundary layer at the ice–ocean in-  
 925 terface fit the descriptions by Baines (2008) for dense downslope flow, except that for  
 926 buoyant upslope flow, everything is upside-down.

927 Current models of subglacial plumes often employ an assumption of continuous en-  
 928 trainment into the plume (Lazeroms et al., 2018; Hewitt, 2020), a process that has so  
 929 far not been well constrained by measurements (Anselin et al., 2023). Our results put  
 930 the validity of this assumption into question. In fact, the subglacial plume in our ide-  
 931 alized 79NG fjord model shows entrainment only for about half of its way along the ice  
 932 tongue, but detrainment afterward. Detrainment is generally not included in current mod-  
 933 els of meltwater plumes. We thus echo the statement by Hewitt (2020) that these mod-  
 934 els might not capture all important dynamics and should be revised.

935 The depth at which meltwater leaves the glacier fjord is not only relevant for the  
 936 export of glacially modified water but also for the development of the ice tongue. Our  
 937 simulations show that most subglacial melting occurs while the subglacial plume is at  
 938 the ice–ocean interface. When the plume detaches, the melt rate drops to almost zero.  
 939 This happens roughly at the same level as the meltwater outflow. Thus, oceanographic  
 940 measurements of the depth of glacially modified water near a glacier fjord can be used  
 941 to infer which part of the glacier tongue is likely to show high basal melt rates. This in-  
 942 formation can be helpful for a decision of where to install measurement stations on a float-  
 943 ing ice tongue to monitor ice thickness changes.

944 At the depth where the subglacial plume propagates away from the ice tongue, the  
 945 vertical coordinate levels in our model accumulate. This ensures that the water prop-  
 946 erties of the plume are preserved over long distances with little spurious mixing. It is achieved  
 947 automatically by the stratification zooming of AVC. No *a priori* knowledge of the po-  
 948 sition of plume detachment is needed, which is an important difference to non-adaptive  
 949 coordinates that can achieve high vertical resolutions in pre-defined regions. Moreover,  
 950 AVC change the vertical layer distribution with time, for example in simulations with  
 951 tides or other time-varying forcings that alter the stratification.

952 With  $z$ -coordinates, which are often used to model the ocean under an ice tongue  
 953 or an ice shelf (e.g., Hellmer & Olbers, 1989; Losch, 2008), it would be difficult to ob-  
 954 tain equally detailed simulations of the cavity circulation and in particular of the sub-  
 955 glacial plume. Due to their step-wise manner of resolving the ice–ocean interface,  $z$ -coordinates  
 956 are usually too diffusive to preserve the plume over longer distances. Without a well-preserved  
 957 plume, an analysis of the entrainment rate as shown in Fig. 6 would not be feasible. An  
 958 insufficient representation of the plume development has also implications on the accu-  
 959 racy of the computation of basal melt rates (Burchard et al., 2022). Furthermore, a good

960 simulation of meltwater export from the fjord into the open ocean demands a good preser-  
 961 vation of the plume properties with minimal spurious mixing. This can be provided by  
 962 AVC while the plume is under the ice. Further development of the adaptive coordinates  
 963 should try to improve also the representation of the outflow after it detached from the  
 964 ice and as it passes under the calving front.

965 While AVC (Hofmeister et al., 2010) have a number of characteristics, the main  
 966 feature used in our setup is their capability to zoom towards stratification. This enables  
 967 high resolutions in the entrainment layers of both plumes and allows the coordinates to  
 968 follow the outflow to a reasonable extent, so that glacially modified water can be trans-  
 969 ported far offshore. This stratification zooming could be combined with other modeling  
 970 approaches like vertical Lagrangian remapping or the Arbitrary Lagrangian-Eulerian (ALE)  
 971 method. In these methods, Lagrangian motion of the model grid is followed by a regrid  
 972 step, in which the coordinate surfaces are moved back to prescribed target positions; the  
 973 physical fields are then mapped onto this new grid in a remap step (Griffies et al., 2020).  
 974 The target coordinate layout could be prescribed based on the ocean stratification in the  
 975 current model state. Such an approach would combine the advantages of ALE with the  
 976 advantages of stratification zooming shown in this paper.

977 As for terrain-following coordinates in general, the calving front presents a chal-  
 978 lenge for AVC. Our setup uses a gentle slope instead of an almost vertical wall at the  
 979 ice front to make sure that the plume is well preserved as it leaves the cavity. This part  
 980 of the ice tongue could possibly be simulated more realistically by a modification of the  
 981 cost function that determines the zooming of AVC. Instead of zooming to stratification  
 982 and the sea surface, it might be advantageous to zoom only to stratification and the ice-  
 983 ocean interface but not to the atmosphere-ocean interface. This way, more layers could  
 984 be available at the calving front to allow a high calving front slope as well as a good preser-  
 985 vation of plume properties. Since AVC (Hofmeister et al., 2010) have not been developed  
 986 with glacier tongues in mind, and this paper presents their first application to an ice cav-  
 987 ity, such a possibility has not yet been implemented. It should however be kept in mind  
 988 that processes at the calving front are strongly nonhydrostatic in nature and therefore  
 989 cannot be sufficiently reproduced with classical ocean models anyway.

990 While our idealized 79NG fjord model shows qualitatively realistic dynamics and  
 991 processes under the glacier tongue, its quantitative results should be taken with a grain  
 992 of salt, as exemplified by our sensitivity study on the sill depth (Section 3.3.4). We ob-  
 993 serve that the melt rate of the ice tongue (Fig. 9) and the strength of the overturning  
 994 circulation in the cavity (Table 2) are very sensitive to the depth of the sill at the fjord  
 995 entrance, which is 300 m in our default setup. However, no single value can be entirely  
 996 realistic, because in the real system, the sill is not at the same depth over the whole fjord  
 997 width (Fig. 1a). The depth of the sill, which is the shallowest point that inflowing wa-  
 998 ter must cross, depends on the path from the open ocean into the cavity. It can be as  
 999 deep as 325 m below sea level but also shallower (see Fig. 1 and Schaffer et al., 2020).  
 1000 Since this cross-fjord variability cannot be reproduced in 2D, the quantitative results of  
 1001 a 2D model can only be approximations.

1002 Another effect that is neglected in the 2D approach is Earth rotation. The inter-  
 1003 nal Rossby radius in the 79NG fjord was estimated to be less than 5 km (Lindeman et  
 1004 al., 2020), so at least four-times smaller than the fjord width (Fig. 1a). This suggests that  
 1005 the plumes are deflected to the right by the Coriolis effect. We expect the inflowing plume  
 1006 to follow the northern boundary of the fjord, while the outflowing plume will be rather  
 1007 along the southern wall. Indeed, satellite measurements show higher subglacial melt rates  
 1008 along the southern boundary (Wilson et al., 2017), which can be caused by a more in-  
 1009 tense subglacial plume in the South. Thus, circulation and melting in the 79NG fjord  
 1010 seem to vary in the transverse direction. However, regarding the sill-controlled inflow  
 1011 of AIW, the situation could be different. The sill is located in a narrow strait of *circa*  
 1012 2 km width, so the inflowing plume is thinner than the internal Rossby radius (Schaf-

1013 fer et al., 2020). It is thus not *a priori* clear, whether rotation plays a dominant role for  
 1014 the sill-controlled inflow. To answer this question, an extension of our setup to a 3D model  
 1015 is necessary.

## 1016 5 Conclusions and Outlook

1017 We developed a numerical ocean model of a glacier fjord in 2D with high horizon-  
 1018 tal and vertical resolution. The fjord and its forcing were built to resemble 79NG in an  
 1019 idealized, analytical way (Fig. 1 and 2). Quantitative results of our default simulation  
 1020 are a good approximation of reality. In particular, the subglacial melt rate and the strength  
 1021 of the overturning circulation are consistent between our model and measurements at  
 1022 the glacier (Table 2). Thanks to the simplicity of the model, its qualitative results (Fig. 3),  
 1023 which we explored further in a sensitivity study, will also hold for other glacier cavities.

1024 Our model shows that the buoyant plume, which develops on the underside of the  
 1025 ice tongue, is responsible for the bulk of subglacial melting. When the plume reaches neu-  
 1026 tral buoyancy and detaches from the ice, basal melting almost stops. At this level, which  
 1027 is about 95 m below sea level in our present-day (default) scenario, the plume transports  
 1028 meltwater out of the fjord towards the open ocean. The detachment depth is set primar-  
 1029 ily by the stratification of the ambient ocean, particularly its salinity (Fig. 7). In between  
 1030 the detachment depth and the sill depth, there are weaker outflows out of the cavity caused  
 1031 by splitting of the subglacial plume (Fig. 5). The plume splits at around 18 km from the  
 1032 grounding line, because the turbulence in the plume is too weak to further entrain am-  
 1033 bient water, so detrainment occurs (Fig. 6).

1034 Furthermore, we confirmed that the depth of the sill at the fjord entrance has a  
 1035 big influence on the melt rate and the overturning strength in the fjord. With a deeper  
 1036 sill, the dense bottom plume brings more warm Atlantic water into the cavity and thus  
 1037 more heat is transported towards the ice tongue (Schaffer et al., 2020), which intensi-  
 1038 fies subglacial melting. In case of 79NG, this sill effect ends at around 350 m depth (Fig. 9).

1039 The two plumes that make up the estuarine circulation in the glacier cavity are re-  
 1040 solved by our model in great detail (Fig. 4 and 6), thanks to the stratification-zooming  
 1041 of AVC (Hofmeister et al., 2010). We showed for the first time that with this modeling  
 1042 approach, a vertical resolution of less than 1 m in the entrainment layer of the buoyant  
 1043 plume under an ice tongue can be achieved (Fig. 4), which is important for the correct  
 1044 representation of subglacial melting and plume development (Burchard et al., 2022). The  
 1045 computational cost compared to non-adaptive  $\sigma$ -coordinates is increased by less than 10 %  
 1046 (Section 2.3), which is much cheaper than increasing the number of vertical layers. Fur-  
 1047 ther advantages of AVC are that they minimize the pressure gradient error (Hofmeister  
 1048 et al., 2010; Gräwe et al., 2015) and that they follow the plumes to some extent, which  
 1049 preserves the properties of the outflowing water mass quite well (Fig. 3). We believe that  
 1050 the application of AVC in more ocean models will mean an improvement to the way pro-  
 1051 cesses under ice tongues and ice shelves are simulated. When stratification zooming is  
 1052 used together with a melt parametrization that is suitable for high vertical resolutions  
 1053 (Burchard et al., 2022), this can refine projections of ice sheet melting and glacier sta-  
 1054 bility.

1055 Given the successful demonstration of AVC in an idealized 2D glacier cavity, a next  
 1056 step should be to extend this setup into a realistic 3D model of the 79NG fjord. This  
 1057 should include resolving the across-fjord dimension with the same high resolution as the  
 1058 along-fjord direction, using the real geometry and topography of the fjord, as well as forc-  
 1059 ing the regional ocean model with actual observational or reanalysis data. Such a setup  
 1060 will allow to study effects that have been neglected so far, *e.g.*, the Coriolis effect, and  
 1061 will back up our qualitative results with accurate quantitative assessments.

## Appendix A Analytical description of the setup

Our setup is built to resemble the 79NG fjord in an idealized way that can be completely described by simple, analytical functions. Here we give the mathematical expressions of these functions for the future use of our setup as a reference test case.

### A1 Model bathymetry

The definition of the default model bathymetry is based on the following points:

- (P1) grounding line ( $x = 0$ ) at  $z_{\text{gline}} = -600$  m,
- (P2) deepest point in the trough at  $(x_{\text{trough}}, z_{\text{trough}}) = (41 \text{ km}, -900 \text{ m})$ ,
- (P3) highest point of the sill at  $(x_{\text{sill}}, z_{\text{sill}}) = (80 \text{ km}, -300 \text{ m})$ ,
- (P4) continental shelf far offshore ( $x \rightarrow \infty$ ) at  $z_{\text{shelf}} = -450$  m,

together with the following conditions on the bottom slope  $dz/dx$ :

- (S1) The slope is zero at the grounding line:  $dz/dx = 0$  for  $x = 0$ .
- (S2) The slope is at most 2.5% in absolute value:  $|dz/dx| \leq s_{\text{max}} = 0.025$  for all  $x \in [0 \text{ km}, 150 \text{ km}]$ .
- (S3) The slope is a continuous function.

The last condition ensures that the bathymetry  $z(x)$  is smooth, the other six conditions are derived from bathymetric measurements (Mayer et al., 2000; Schaffer et al., 2020), see Fig. 1. The combination of these seven conditions fully defines the glacier cavity as the concatenation of a third-order polynomial for the grounding line and the trough, a second-order polynomial for the sill, and a first-order polynomial in between, as explained in the following. With a choice of the transition point from sill to continental shelf (given below), also the exponentially decreasing shelf is fixed.

Conditions (P1,P2,S1) imply that the third-order polynomial going from the grounding line through the trough is

$$z(x) = a_{\text{trough}}x^3 + b_{\text{trough}}x^2 + z_{\text{gline}}, \text{ with} \quad (\text{A1})$$

$$b_{\text{trough}} = 3 \frac{z_{\text{trough}} - z_{\text{gline}}}{(x_{\text{trough}})^2}, \text{ and} \quad (\text{A2})$$

$$a_{\text{trough}} = -\frac{2}{3} \frac{b_{\text{trough}}}{x_{\text{trough}}}. \quad (\text{A3})$$

In consequence of (S2), the trough ends at  $x_0$  such that

$$\frac{dz}{dx}(x_0) = 3a_{\text{trough}}x_0^2 + 2b_{\text{trough}}x_0 = s_{\text{max}}, \text{ where} \quad (\text{A4})$$

$$z_0 = z(x_0) = a_{\text{trough}}x_0^3 + b_{\text{trough}}x_0^2 + z_{\text{gline}}. \quad (\text{A5})$$

From this point onward, the bathymetry is described by an (affine) linear function with slope  $s_{\text{max}}$  (S2,S3):

$$z(x) = z_0 + s_{\text{max}}(x - x_0). \quad (\text{A6})$$

The upper end point of this slope,  $(x_1, z_1)$ , must be chosen such that (S3) is fulfilled for the parabolic sill defined by (P3) and starting at  $(x_1, z_1)$ :

$$z(x) = \frac{a_{\text{sill}}}{2}(x - x_{\text{sill}})^2 + z_{\text{sill}}, \text{ with} \quad (\text{A7})$$

$$a_{\text{sill}} = \frac{s_{\text{max}}}{x_1 - x_{\text{sill}}}. \quad (\text{A8})$$

As eastern end point of the parabola,  $(x_2, z_2)$ , we choose the position where its slope equals  $-s_{\text{max}}/2$ . At this point, an exponential function with the same slope starts (S3) and de-

1101 creases in accordance with (P4):

$$1102 \quad z(x) = a_{\text{shelf}} \exp(b_{\text{shelf}}x) + z_{\text{shelf}}, \text{ with} \quad (A9)$$

$$1103 \quad a_{\text{shelf}} = \frac{z_2 - z_{\text{shelf}}}{\exp(b_{\text{shelf}}x_2)}, \text{ and} \quad (A10)$$

$$1104 \quad b_{\text{shelf}} = a_{\text{sill}} \frac{x_2 - x_{\text{sill}}}{z_2 - z_{\text{shelf}}}. \quad (A11)$$

1105 In the sensitivity experiment with the sill at  $z_{\text{sill}} = -400$  m (Section 3.3.4), we  
 1106 put the connection between parabolic sill and exponential shelf at the point where the  
 1107 bottom slope equals  $-s_{\text{max}}/3$ , to avoid  $z_2 < z_{\text{shelf}}$ . In the scenario without a sill, the  
 1108 linear slope connects directly to an exponentially increasing shelf at  $z_1 = -600$  m.

1109 A Python implementation of the here-explained mathematical expressions is pro-  
 1110 vided with the model setup (Reinert, 2023b) that belongs to this paper.

## 1111 A2 Model ice topography

1112 The position of the lower ice edge is defined in our model in two parts. Between  
 1113 the grounding line and the calving front, we use a hyperbolic tangent shape:

$$1114 \quad \eta(x) = a_{\text{ice}} \tanh[b_{\text{ice}}(x - c_{\text{ice}})] + d_{\text{ice}}. \quad (A12)$$

1115 A reasonable choice of the parameters and a good fit to the ice shape near the ground-  
 1116 ing line (Fig. 1b) is obtained if the maximum ice slope is at the grounding line ( $x = 0$ )  
 1117 and has a value of  $\max(d\eta/dx) = s_{\text{max}} = 0.025$ . This greatly simplifies the expres-  
 1118 sion, since  $c_{\text{ice}} = 0$ , thus  $d_{\text{ice}} = z_{\text{gline}}$ , and  $b_{\text{ice}} = s_{\text{max}}/a_{\text{ice}}$ . We further take  $a_{\text{ice}} =$   
 1119  $525$  m, so that the ice topography converges to  $\eta = -75$  m (Fig. 1b). The Python code  
 1120 for the model setup (Reinert, 2023b) provided with this paper also implements the op-  
 1121 tion of a maximum slope at a position  $c_{\text{ice}}$  different from the grounding line (not used  
 1122 in this paper), but this requires computing  $a_{\text{ice}}$  numerically to fulfill the condition that  
 1123  $\eta$  converges to  $-75$  m in eastward direction.

1124 After the calving front ( $x = 75$  km), we linearly connect the lower ice edge with  
 1125 sea level. The linear connection has a slope of 1%, which ensures a low perturbation of  
 1126 the subglacial plume as it passes under the calving front (Fig. 3). With a modification  
 1127 of the vertical coordinates as discussed in Section 4, a higher slope might be feasible.

## 1128 A3 Model stratification

1129 Our model uses as initial and boundary conditions the same horizontally homo-  
 1130 geneous stratification. The stratification is defined by specifying temperature and salin-  
 1131 ity at three vertical positions, with a linear interpolation of the values in between and  
 1132 a constant extrapolation below. In our default scenario, the salinity-values are  $S(z =$   
 1133  $0) = 29 \text{ g kg}^{-1}$ ,  $S(z = -100 \text{ m}) = 34 \text{ g kg}^{-1}$ ,  $S(z = -300 \text{ m}) = 35 \text{ g kg}^{-1}$  (Fig. 2a).  
 1134 The temperature-values are  $\theta(z = 0) = -1.5^\circ\text{C}$ ,  $\theta(z = -100 \text{ m}) = -1.0^\circ\text{C}$ ,  $\theta(z =$   
 1135  $-300 \text{ m}) = 1.5^\circ\text{C}$  (Fig. 2b). The modified values in the sensitivity study are given in  
 1136 Sections 3.3.1 and 3.3.2.

## 1137 Open Research

1138 The model setup can be downloaded from <https://doi.org/10.5281/zenodo.7755753>  
 1139 (Reinert, 2023b) together with instructions how to reproduce the simulations presented  
 1140 in this paper. The corresponding GETM source code can be downloaded from [https://](https://doi.org/10.5281/zenodo.7741925)  
 1141 [doi.org/10.5281/zenodo.7741925](https://doi.org/10.5281/zenodo.7741925) (Klingbeil, 2023). The model output generated by  
 1142 this code and presented in this manuscript can be downloaded from [https://doi.org/](https://doi.org/10.5281/zenodo.7755908)  
 1143 [10.5281/zenodo.7755908](https://doi.org/10.5281/zenodo.7755908) (Reinert, 2023a).

1144 This paper contains no unpublished observational data. Figure 1 uses topography  
 1145 data published by Mayer et al. (2018) and Schaffer et al. (2019). Figure 2 shows CTD  
 1146 profile 115-1 from *Polarstern* cruise PS109 published by Kanzow et al. (2018).

## 1147 Acknowledgments

1148 The work of this study has been supported by the collaborative research project GROCE  
 1149 (Greenland Ice Sheet–Ocean Interaction) funded by the German Federal Ministry of Ed-  
 1150 ucation and Research (BMBF, grant 03F0855E). This paper is a contribution to the projects  
 1151 M5 (Reducing Spurious Mixing and Energetic Inconsistencies in Realistic Ocean-Modelling  
 1152 Applications) and S1 (Diagnosis and Metrics in Climate Models) of the collaborative re-  
 1153 search center TRR 181 “Energy Transfers in Atmosphere and Ocean” funded by the Ger-  
 1154 man Research Foundation (DFG, project 274762653). ML is supported by ECAS-BALTIC  
 1155 funded by the German Federal Ministry of Education and Research (BMBF, grant 03F0860H).  
 1156 We thank Sarah Vierling (Amherst College, Massachusetts, USA) for extending the code  
 1157 used to create the model setup and for running many sensitivity experiments during an  
 1158 internship supervised by Markus Reinert in Hans Burchard’s lab, funded by the German  
 1159 Academic Exchange Service (DAAD) in the program “RISE Germany”. We thank three  
 1160 anonymous reviewers and the editor for their efforts, which were of great help in improv-  
 1161 ing the manuscript. Figures in this paper use the colormaps of the cmocean package (Thyng  
 1162 et al., 2016).

## 1163 References

- 1164 Anselin, J., Reed, B. C., Jenkins, A., & Green, J. a. M. (2023). Ice Shelf Basal  
 1165 Melt Sensitivity to Tide-Induced Mixing Based on the Theory of Sub-  
 1166 glacial Plumes. *Journal of Geophysical Research: Oceans*, 128(4). doi:  
 1167 10.1029/2022JC019156
- 1168 Arneborg, L., Fiekas, V., Umlauf, L., & Burchard, H. (2007). Gravity Cur-  
 1169 rent Dynamics and Entrainment—A Process Study Based on Observa-  
 1170 tions in the Arkona Basin. *Journal of Physical Oceanography*, 37(8). doi:  
 1171 10.1175/JPO3110.1
- 1172 Aschwanden, A., Fahnestock, M. A., Truffer, M., Brinkerhoff, D. J., Hock, R.,  
 1173 Khroulev, C., ... Khan, S. A. (2019). Contribution of the Greenland Ice  
 1174 Sheet to sea level over the next millennium. *Science Advances*, 5(6). doi:  
 1175 10.1126/sciadv.aav9396
- 1176 Baines, P. G. (2008). Mixing in downslope flows in the ocean - plumes versus gravity  
 1177 currents. *Atmosphere-Ocean*, 46(4). doi: 10.3137/ao.460402
- 1178 Burchard, H., & Baumert, H. (1995). On the performance of a mixed-layer model  
 1179 based on the  $\kappa$ - $\epsilon$  turbulence closure. *Journal of Geophysical Research: Oceans*,  
 1180 100(C5). doi: 10.1029/94JC03229
- 1181 Burchard, H., & Beckers, J.-M. (2004). Non-uniform adaptive vertical grids in one-  
 1182 dimensional numerical ocean models. *Ocean Modelling*, 6(1). doi: 10.1016/  
 1183 S1463-5003(02)00060-4
- 1184 Burchard, H., & Bolding, K. (2002). *GETM – A General Estuarine Transport Model*  
 1185 (Tech. Rep. No. EUR 20253 EN). European Commission.
- 1186 Burchard, H., Bolding, K., Jenkins, A., Losch, M., Reinert, M., & Umlauf, L. (2022).  
 1187 The Vertical Structure and Entrainment of Subglacial Melt Water Plumes.  
 1188 *JAMES*, 14(3). doi: 10.1029/2021MS002925
- 1189 Burchard, H., Bolding, K., & Villarreal, M. R. (1999). *GOTM, a general ocean tur-  
 1190 bulance model: Theory, implementation and test cases*. Space Applications In-  
 1191 stitute.
- 1192 Burchard, H., & Hetland, R. D. (2010). Quantifying the Contributions of Tidal  
 1193 Straining and Gravitational Circulation to Residual Circulation in Periodically  
 1194 Stratified Tidal Estuaries. *Journal of Physical Oceanography*, 40(6). doi:

- 10.1175/2010JPO4270.1
- 1195 Burchard, H., & Petersen, O. (1997). Hybridization between sigma- and z-co-  
1196 ordinates for improving the internal pressure gradient calculation in marine  
1197 models with steep bottom slopes. *International Journal for Numerical Meth-*  
1198 *ods in Fluids*, 25(9). doi: 10.1002/(SICI)1097-0363(19971115)25:9<1003::  
1199 AID-FLD600>3.0.CO;2-E
- 1200 Chegini, F., Holtermann, P., Kerimoglu, O., Becker, M., Kreuz, M., Klingbeil, K., ...  
1201 Burchard, H. (2020). Processes of Stratification and Destratification During  
1202 An Extreme River Discharge Event in the German Bight ROFI. *Journal of*  
1203 *Geophysical Research: Oceans*, 125(8). doi: 10.1029/2019JC015987
- 1204 Cheng, Y., Canuto, V. M., & Howard, A. M. (2002). An Improved Model for the  
1205 Turbulent PBL. *Journal of the Atmospheric Sciences*, 59(9). doi: 10.1175/  
1206 1520-0469(2002)059<1550:AIMFTT>2.0.CO;2
- 1207 Christmann, J., Helm, V., Khan, S. A., Kleiner, T., Müller, R., Morlighem, M.,  
1208 ... Humbert, A. (2021). Elastic deformation plays a non-negligible role  
1209 in Greenland’s outlet glacier flow. *Commun Earth Environ*, 2(1). doi:  
1210 10.1038/s43247-021-00296-3
- 1211 Goldberg, D., Holland, D. M., & Schoof, C. (2009). Grounding line movement and  
1212 ice shelf buttressing in marine ice sheets. *Journal of Geophysical Research:*  
1213 *Earth Surface*, 114(F4). doi: 10.1029/2008JF001227
- 1214 Gräwe, U., Holtermann, P., Klingbeil, K., & Burchard, H. (2015). Advantages of  
1215 vertically adaptive coordinates in numerical models of stratified shelf seas.  
1216 *Ocean Modelling*, 92. doi: 10.1016/j.ocemod.2015.05.008
- 1217 Griffies, S. M., Adcroft, A., & Hallberg, R. W. (2020). A Primer on the Vertical  
1218 Lagrangian-Remap Method in Ocean Models Based on Finite Volume Gener-  
1219 alized Vertical Coordinates. *Journal of Advances in Modeling Earth Systems*,  
1220 12(10). doi: 10.1029/2019MS001954
- 1221 Grosfeld, K., & Gerdes, R. (1998). Circulation beneath the Filchner Ice Shelf,  
1222 Antarctica, and its sensitivity to changes in the oceanic environment: A case-  
1223 study. *Annals of Glaciology*, 27. doi: 10.3189/1998AoG27-1-99-104
- 1224 Gwyther, D. E., Kusahara, K., Asay-Davis, X. S., Dinniman, M. S., & Galton-  
1225 Fenzi, B. K. (2020). Vertical processes and resolution impact ice shelf  
1226 basal melting: A multi-model study. *Ocean Modelling*, 147. doi: 10.1016/  
1227 j.ocemod.2020.101569
- 1228 Haney, R. L. (1991). On the Pressure Gradient Force over Steep Topography in  
1229 Sigma Coordinate Ocean Models. *Journal of Physical Oceanography*, 21(4).  
1230 doi: 10.1175/1520-0485(1991)021<0610:OTPGFO>2.0.CO;2
- 1231 Hellmer, H. H., & Olbers, D. J. (1989). A two-dimensional model for the thermo-  
1232 haline circulation under an ice shelf. *Antarctic Science*, 1(4). doi: 10.1017/  
1233 S0954102089000490
- 1234 Hewitt, I. J. (2020). Subglacial Plumes. *Annual Review of Fluid Mechanics*, 52(1).  
1235 doi: 10.1146/annurev-fluid-010719-060252
- 1236 Hofmeister, R., Burchard, H., & Beckers, J.-M. (2010). Non-uniform adaptive ver-  
1237 tical grids for 3D numerical ocean models. *Ocean Modelling*, 33(1). doi: 10  
1238 .1016/j.ocemod.2009.12.003
- 1239 Holland, D. M., & Jenkins, A. (1999). Modeling Thermodynamic Ice–Ocean Interac-  
1240 tions at the Base of an Ice Shelf. *J. Phys. Oceanogr.*, 29(8). doi: 10.1175/1520  
1241 -0485(1999)029<1787:MTIOIA>2.0.CO;2
- 1242 Holland, P. R., & Feltham, D. L. (2006). The Effects of Rotation and Ice Shelf  
1243 Topography on Frazil-Laden Ice Shelf Water Plumes. *Journal of Physical*  
1244 *Oceanography*, 36(12). doi: 10.1175/JPO2970.1
- 1245 Holland, P. R., Jenkins, A., & Holland, D. M. (2008). The Response of Ice Shelf  
1246 Basal Melting to Variations in Ocean Temperature. *Journal of Climate*,  
1247 21(11). doi: 10.1175/2007JCLI1909.1
- 1248 Horwath, M., Gutknecht, B. D., Cazenave, A., Palanisamy, H. K., Marti, F.,  
1249

- 1250 Marzeion, B., ... Benveniste, J. (2022). Global sea-level budget and ocean-  
 1251 mass budget, with a focus on advanced data products and uncertainty char-  
 1252 terisation. *Earth System Science Data*, *14*(2). doi: 10.5194/essd-14-411-2022
- 1253 Huang, R. X. (1993). Real Freshwater Flux as a Natural Boundary Condition  
 1254 for the Salinity Balance and Thermohaline Circulation Forced by Evapo-  
 1255 ration and Precipitation. *Journal of Physical Oceanography*, *23*(11). doi:  
 1256 10.1175/1520-0485(1993)023{(\$)}2428:RFFAAN{(\$)}2.0.CO;2
- 1257 Humbert, A., Christmann, J., Corr, H. F. J., Helm, V., Höyns, L.-S., Hofstede, C.,  
 1258 ... Zeising, O. (2022). On the evolution of an ice shelf melt channel at the  
 1259 base of Filchner Ice Shelf, from observations and viscoelastic modeling. *The*  
 1260 *Cryosphere*, *16*(10). doi: 10.5194/tc-16-4107-2022
- 1261 Inall, M. E., & Gillibrand, P. A. (2010). The physics of mid-latitude fjords: A re-  
 1262 view. *Geological Society, London, Special Publications*, *344*(1). doi: 10.1144/  
 1263 SP344.3
- 1264 IOC, SCOR, & IAPSO. (2010). The international thermodynamic equation of sea-  
 1265 water – 2010: Calculation and use of thermodynamic properties. *Intergovern-*  
 1266 *mental Oceanographic Commission, Manuals and Guides No. 56, UNESCO.*  
 1267 doi: 10.25607/OBP-1338
- 1268 IPCC. (2022). Summary for policymakers [Book Section]. In H. O. Pörtner et al.  
 1269 (Eds.), *Climate change 2022: Impacts, adaptation, and vulnerability. contribu-*  
 1270 *tion of working group ii to the sixth assessment report of the intergovernmental*  
 1271 *panel on climate change* (p. In Press). Cambridge, UK: Cambridge University  
 1272 Press. (In Press)
- 1273 Jenkins, A. (1991). A one-dimensional model of ice shelf-ocean interaction. *Journal*  
 1274 *of Geophysical Research: Oceans*, *96*(C11). doi: 10.1029/91JC01842
- 1275 Jenkins, A. (2011). Convection-Driven Melting near the Grounding Lines of Ice  
 1276 Shelves and Tidewater Glaciers. *J. Phys. Oceanogr.*, *41*(12). doi: 10.1175/JPO  
 1277 -D-11-03.1
- 1278 Jenkins, A., Hellmer, H. H., & Holland, D. M. (2001). The Role of Meltwa-  
 1279 ter Advection in the Formulation of Conservative Boundary Conditions at  
 1280 an Ice–Ocean Interface. *Journal of Physical Oceanography*, *31*(1). doi:  
 1281 10.1175/1520-0485(2001)031{(\$)}0285:TROMAI{(\$)}2.0.CO;2
- 1282 Jourdain, N. C., Mathiot, P., Merino, N., Durand, G., Le Sommer, J., Spence, P., ...  
 1283 Madec, G. (2017). Ocean circulation and sea-ice thinning induced by melting  
 1284 ice shelves in the Amundsen Sea. *Journal of Geophysical Research: Oceans*,  
 1285 *122*(3). doi: 10.1002/2016JC012509
- 1286 Kanzow, T., Schaffer, J., & Rohardt, G. (2018). Physical oceanography during  
 1287 POLARSTERN cruise PS109 (ARK-XXXI/4). *Alfred Wegener Institute,*  
 1288 *Helmholtz Centre for Polar and Marine Research, Bremerhaven.* (Dataset)  
 1289 doi: 10.1594/PANGAEA.885358
- 1290 Kappelsberger, M. T., Strößenreuther, U., Scheinert, M., Horwath, M., Groh, A.,  
 1291 Knöfel, C., ... Khan, S. A. (2021). Modeled and Observed Bedrock Dis-  
 1292 placements in North-East Greenland Using Refined Estimates of Present-Day  
 1293 Ice-Mass Changes and Densified GNSS Measurements. *Journal of Geophysical*  
 1294 *Research: Earth Surface*, *126*(4). doi: 10.1029/2020JF005860
- 1295 Klingbeil, K. (2023). *Source code for the coastal ocean model GETM (glacial\_ice*  
 1296 *branch)*. Zenodo. (Model code) doi: 10.5281/zenodo.7741925
- 1297 Klingbeil, K., & Burchard, H. (2013). Implementation of a direct nonhydrostatic  
 1298 pressure gradient discretisation into a layered ocean model. *Ocean Modelling*,  
 1299 *65*. doi: 10.1016/j.ocemod.2013.02.002
- 1300 Klingbeil, K., Lemarié, F., Debreu, L., & Burchard, H. (2018). The numerics of  
 1301 hydrostatic structured-grid coastal ocean models: State of the art and future  
 1302 perspectives. *Ocean Modelling*, *125*. doi: 10.1016/j.ocemod.2018.01.007
- 1303 Klingbeil, K., Mohammadi-Aragh, M., Gräwe, U., & Burchard, H. (2014). Quantifi-  
 1304 cation of spurious dissipation and mixing – Discrete variance decay in a Finite-

- 1305 Volume framework. *Ocean Modelling*, 81. doi: 10.1016/j.ocemod.2014.06.001  
 1306 Lazeroms, W. M. J., Jenkins, A., Gudmundsson, G. H., & van de Wal, R. S. W.  
 1307 (2018). Modelling present-day basal melt rates for Antarctic ice shelves using  
 1308 a parametrization of buoyant meltwater plumes. *The Cryosphere*, 12(1). doi:  
 1309 10.5194/tc-12-49-2018
- 1310 Li, Q., Bruggeman, J., Burchard, H., Klingbeil, K., Umlauf, L., & Bolding, K.  
 1311 (2021). Integrating CVMix into GOTM (v6.0): A consistent framework for  
 1312 testing, comparing, and applying ocean mixing schemes. *Geoscientific Model  
 1313 Development*, 14(7). doi: 10.5194/gmd-14-4261-2021
- 1314 Lindeman, M. R., Straneo, F., Wilson, N. J., Toole, J. M., Krishfield, R. A., Beard,  
 1315 N. L., ... Schaffer, J. (2020). Ocean Circulation and Variability Beneath  
 1316 Nioghalvfjærdsbræ (79 North Glacier) Ice Tongue. *Journal of Geophysical  
 1317 Research: Oceans*, 125(8). doi: 10.1029/2020JC016091
- 1318 Losch, M. (2008). Modeling ice shelf cavities in a z coordinate ocean general circulation  
 1319 model. *Journal of Geophysical Research: Oceans*, 113(C8). doi: 10.1029/  
 1320 2007JC004368
- 1321 Mayer, C., Reeh, N., Jung-Rothenhäusler, F., Huybrechts, P., & Oerter, H.  
 1322 (2018). Main ice thickness and bedrock elevation data of Nioghalvfjærds-  
 1323 fjorden Glacier from seismic investigations in 1997/1998. *In supplement to:  
 1324 Mayer, C et al. (2000): The subglacial cavity and implied dynamics under  
 1325 Nioghalvfjærdsfjorden Glacier, NE-Greenland. Geophysical Research Letters,*  
 1326 *27(15), 2289-2292, https://doi.org/10.1029/2000GL011514.* (Dataset) doi:  
 1327 10.1594/PANGAEA.891368
- 1328 Mayer, C., Reeh, N., Jung-Rothenhäusler, F., Huybrechts, P., & Oerter, H.  
 1329 (2000). The subglacial cavity and implied dynamics under Nioghalvfjærds-  
 1330 fjorden Glacier, NE-Greenland. *Geophysical Research Letters*, 27(15). doi:  
 1331 10.1029/2000GL011514
- 1332 Muilwijk, M., Straneo, F., Slater, D. A., Smedsrud, L. H., Holte, J., Wood, M.,  
 1333 ... Harden, B. (2022). Export of Ice Sheet Meltwater from Upernavik  
 1334 Fjord, West Greenland. *Journal of Physical Oceanography*, 52(3). doi:  
 1335 10.1175/JPO-D-21-0084.1
- 1336 Payne, A. J., Holland, P. R., Shepherd, A. P., Rutt, I. C., Jenkins, A., & Joughin,  
 1337 I. (2007). Numerical modeling of ocean-ice interactions under Pine Island  
 1338 Bay's ice shelf. *Journal of Geophysical Research: Oceans*, 112(C10). doi:  
 1339 10.1029/2006JC003733
- 1340 Reinert, M. (2023a). *Output files of the 2DV-model for the 79NG fjord.* Zenodo.  
 1341 (Dataset) doi: 10.5281/zenodo.7755908
- 1342 Reinert, M. (2023b). *Setup files of the 2DV-model for the 79NG fjord.* Zenodo.  
 1343 (Model setup) doi: 10.5281/zenodo.7755753
- 1344 Rignot, E., & Steffen, K. (2008). Channelized bottom melting and stabil-  
 1345 ity of floating ice shelves. *Geophysical Research Letters*, 35(2). doi:  
 1346 10.1029/2007GL031765
- 1347 Schaffer, J., Kanzow, T., von Appen, W.-J., von Albedyll, L., Arndt, J. E.,  
 1348 & Roberts, D. H. (2020). Bathymetry constrains ocean heat supply  
 1349 to Greenland's largest glacier tongue. *Nature Geoscience*, 13(3). doi:  
 1350 10.1038/s41561-019-0529-x
- 1351 Schaffer, J., Timmermann, R., Arndt, J. E., Rosier, S. H. R., Anker, P. G. D.,  
 1352 Callard, S. L., ... Roberts, D. H. (2019). An update to Greenland and  
 1353 Antarctic ice sheet topography, cavity geometry, and global bathymetry  
 1354 (RTopo-2.0.4). *Supplement to: Schaffer, Janin; Kanzow, Torsten; von Appen,  
 1355 Wilken-Jon; von Albedyll, Luisa; Arndt, Jan Erik; Roberts, David H (2020):  
 1356 Bathymetry constrains ocean heat supply to Greenland's largest glacier tongue.*  
 1357 *Nature Geoscience*, 13(3), 227-231, [https://doi.org/10.1038/s41561-019-0529-](https://doi.org/10.1038/s41561-019-0529-x)  
 1358 *x.* (Dataset) doi: 10.1594/PANGAEA.905295
- 1359 Schaffer, J., von Appen, W.-J., Dodd, P. A., Hofstede, C., Mayer, C., de Steur, L.,

- 1360 & Kanzow, T. (2017). Warm water pathways toward Nioghalvfjærdsfjorden  
1361 Glacier, Northeast Greenland. *Journal of Geophysical Research: Oceans*,  
1362 *122*(5). doi: 10.1002/2016JC012462
- 1363 Shepherd, A., Wingham, D., & Rignot, E. (2004). Warm ocean is eroding  
1364 West Antarctic Ice Sheet. *Geophysical Research Letters*, *31*(23). doi:  
1365 10.1029/2004GL021106
- 1366 Slater, D. A., & Straneo, F. (2022). Submarine melting of glaciers in Greenland am-  
1367 plified by atmospheric warming. *Nat. Geosci.* doi: 10.1038/s41561-022-01035-  
1368 9
- 1369 Stolzenberger, S., Rietbroek, R., Wekerle, C., Uebbing, B., & Kusche, J. (2022).  
1370 Simulated Signatures of Greenland Melting in the North Atlantic: A  
1371 Model Comparison With Argo Floats, Satellite Observations, and Ocean  
1372 Reanalysis. *Journal of Geophysical Research: Oceans*, *127*(11). doi:  
1373 10.1029/2022JC018528
- 1374 Straneo, F., & Cenedese, C. (2015). The Dynamics of Greenland’s Glacial Fjords  
1375 and Their Role in Climate. *Annu. Rev. Mar. Sci.*, *7*(1). doi: 10.1146/annurev-  
1376 -marine-010213-135133
- 1377 Thyng, K. M., Greene, C. A., Hetland, R. D., Zimmerle, H. M., & DiMarco, S. F.  
1378 (2016). True Colors of Oceanography: Guidelines for Effective and Accurate  
1379 Colormap Selection. *Oceanography*, *29*(3).
- 1380 Timmermann, R., Wang, Q., & Hellmer, H. H. (2012). Ice-shelf basal melting in  
1381 a global finite-element sea-ice/ice-shelf/ocean model. *Annals of Glaciology*,  
1382 *53*(60). doi: 10.3189/2012AoG60A156
- 1383 Umlauf, L. (2009). The Description of Mixing in Stratified Layers without Shear in  
1384 Large-Scale Ocean Models. *Journal of Physical Oceanography*, *39*(11). doi: 10  
1385 .1175/2009JPO4006.1
- 1386 Umlauf, L., Arneborg, L., Hofmeister, R., & Burchard, H. (2010). Entrainment  
1387 in Shallow Rotating Gravity Currents: A Modeling Study. *Journal of Physical  
1388 Oceanography*, *40*(8). doi: 10.1175/2010JPO4367.1
- 1389 Umlauf, L., & Burchard, H. (2005). Second-order turbulence closure models for geo-  
1390 physical boundary layers. A review of recent work. *Continental Shelf Research*,  
1391 *25*(7). doi: 10.1016/j.csr.2004.08.004
- 1392 Vallis, G. K. (1992). Mechanisms and Parameterizations of Geostrophic Adjustment  
1393 and a Variational Approach to Balanced Flow. *Journal of the Atmospheric Sci-  
1394 ences*, *49*(13). doi: 10.1175/1520-0469(1992)049{1144:MAPOGA}2.0  
1395 .CO;2
- 1396 Wilson, N., Straneo, F., & Heimbach, P. (2017). Satellite-derived submarine melt  
1397 rates and mass balance (2011–2015) for Greenland’s largest remaining ice  
1398 tongues. *The Cryosphere*, *11*(6). doi: 10.5194/tc-11-2773-2017
- 1399 Xu, Y., Rignot, E., Fenty, I., Menemenlis, D., & Flexas, M. M. (2013). Subaque-  
1400 ous melting of Store Glacier, west Greenland from three-dimensional, high-  
1401 resolution numerical modeling and ocean observations. *Geophysical Research  
1402 Letters*, *40*(17). doi: 10.1002/grl.50825
- 1403 Xu, Y., Rignot, E., Menemenlis, D., & Koppes, M. (2012). Numerical experiments  
1404 on subaqueous melting of Greenland tidewater glaciers in response to ocean  
1405 warming and enhanced subglacial discharge. *Annals of Glaciology*, *53*(60). doi:  
1406 10.3189/2012AoG60A139